

## Mysterious $\text{SiB}_3$ : Identifying the Relation between $\alpha$ - and $\beta$ - $\text{SiB}_3$

Daniel Eklöf,<sup>†</sup> Andreas Fischer,<sup>‡</sup> Annop Ektarawong,<sup>§,||</sup> Aleksander Jaworski,<sup>†</sup><sup>ID</sup> Andrew J. Pell,<sup>†</sup><sup>ID</sup> Jekabs Grins,<sup>†</sup> Sergei I. Simak,<sup>†</sup> Björn Alling,<sup>†</sup> Yang Wu,<sup>#</sup> Michael Widom,<sup>▽</sup><sup>ID</sup> Wolfgang Scherer,<sup>‡</sup><sup>ID</sup> and Ulrich Häussermann<sup>\*,†</sup><sup>ID</sup>

<sup>†</sup>Department of Materials and Environmental Chemistry, Stockholm University, S-10691 Stockholm, Sweden

<sup>‡</sup>Department of Physics, Augsburg University, D-86135 Augsburg, Germany

<sup>§</sup>Extreme Conditions Physics Research Laboratory, Physics of Energy Materials Research Unit, Department of Physics, Faculty of Science, Chulalongkorn University, Bangkok 10330, Thailand

<sup>||</sup>Thailand Center of Excellence in Physics, Commission on Higher Education, 328 Si Ayutthaya Road, Bangkok 10400, Thailand

<sup>#</sup>Theoretical Physics Division, Department of Physics, Chemistry and Biology (IFM), Linköping University, SE-581 83 Linköping, Sweden

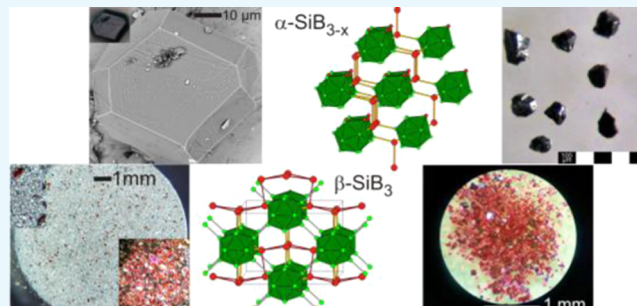
<sup>\*</sup>Department of Mechanical Engineering and Tsinghua-Foxconn Nanotechnology Research Center, Tsinghua University, Beijing 10084, China

<sup>▽</sup>Department of Physics, Carnegie Mellon University, Pittsburgh, Pennsylvania 15213, United States

### S Supporting Information

**ABSTRACT:** Binary silicon boride  $\text{SiB}_3$  has been reported to occur in two forms, as disordered and nonstoichiometric  $\alpha$ - $\text{SiB}_{3-x}$  which relates to the  $\alpha$ -rhombohedral phase of boron, and as strictly ordered and stoichiometric  $\beta$ - $\text{SiB}_3$ . Similar to other boron-rich icosahedral solids, these  $\text{SiB}_3$  phases represent potentially interesting refractory materials. However, their thermal stability, formation conditions, and thermodynamic relation are poorly understood. Here, we map the formation conditions of  $\alpha$ - $\text{SiB}_{3-x}$  and  $\beta$ - $\text{SiB}_3$  and analyze their relative thermodynamic stabilities.  $\alpha$ - $\text{SiB}_{3-x}$  is metastable (with respect to  $\beta$ - $\text{SiB}_3$  and Si), and its formation is kinetically driven. Pure polycrystalline bulk samples may be obtained within hours when heating stoichiometric mixtures of elemental silicon and boron at temperatures 1200–1300 °C. At the same time,  $\alpha$ - $\text{SiB}_{3-x}$  decomposes into  $\text{SiB}_6$  and Si, and optimum time-temperature synthesis conditions represent a trade-off between rates of formation and decomposition. The formation of stable  $\beta$ - $\text{SiB}_3$  was observed after prolonged treatment (days to weeks) of elemental mixtures with ratios Si/B = 1:1–1:4 at temperatures 1175–1200 °C. The application of high pressures greatly improves the kinetics of  $\text{SiB}_3$  formation and allows decoupling of  $\text{SiB}_3$  formation from decomposition. Quantitative formation of  $\beta$ - $\text{SiB}_3$  was seen at 1100 °C for samples pressurized to 5.5–8 GPa.  $\beta$ - $\text{SiB}_3$  decomposes peritectoidally at temperatures between 1250 and 1300 °C. The highly ordered nature of  $\beta$ - $\text{SiB}_3$  is reflected in its Raman spectrum, which features narrow and distinct lines. In contrast, the Raman spectrum of  $\alpha$ - $\text{SiB}_{3-x}$  is characterized by broad bands, which show a clear relation to the vibrational modes of isostructural, ordered  $\text{B}_6\text{P}$ . The detailed composition and structural properties of disordered  $\alpha$ - $\text{SiB}_{3-x}$  were ascertained by a combination of single-crystal X-ray diffraction and <sup>29</sup>Si magic angle spinning NMR experiments. Notably, the compositions of polycrystalline bulk samples (obtained at  $T \leq 1200$  °C) and single crystal samples (obtained from Si-rich molten Si–B mixtures at  $T > 1400$  °C) are different,  $\text{SiB}_{2.93(7)}$  and  $\text{SiB}_{2.64(2)}$ , respectively. The incorporation of Si in the polar position of  $\text{B}_{12}$  icosahedra results in highly strained cluster units. This disorder feature was accounted for in the refined crystal structure model by splitting the polar position into three sites. The electron-precise composition of  $\alpha$ - $\text{SiB}_{3-x}$  is  $\text{SiB}_{2.5}$  and corresponds to the incorporation of, on average, two Si atoms in each  $\text{B}_{12}$  icosahedron. Accordingly,  $\alpha$ - $\text{SiB}_{3-x}$  constitutes a mixture of  $\text{B}_{10}\text{Si}_2$  and  $\text{B}_{11}\text{Si}$  clusters. The structural and phase stability of  $\alpha$ - $\text{SiB}_{3-x}$  were explored using a first-principles cluster expansion. The most stable composition at 0 K is  $\text{SiB}_{2.5}$ , which however is unstable with respect to the decomposition  $\beta$ - $\text{SiB}_3 + \text{Si}$ . Modeling of the configurational and vibrational entropies suggests that  $\alpha$ - $\text{SiB}_{3-x}$  only becomes more stable than  $\beta$ - $\text{SiB}_3$  at temperatures above its decomposition into  $\text{SiB}_6$  and Si. Hence, we conclude that  $\alpha$ - $\text{SiB}_{3-x}$  is metastable at all temperatures.

continued...



Received: August 23, 2019

Accepted: October 10, 2019

Published: November 1, 2019

Density functional theory electronic structure calculations yield band gaps of similar size for electron-precise  $\alpha\text{-SiB}_{2.5}$  and  $\beta\text{-SiB}_3$ , whereas  $\alpha\text{-SiB}_3$  represents a p-type conductor.

## 1. INTRODUCTION

The semiconducting  $\alpha$ -rhombohedral phase of boron ( $\alpha\text{-B}_{12}$ ) is parent to a family of refractory materials—sometimes referred to as “ $\alpha\text{-B}_{12}$  derived icosahedral boron-rich solids”<sup>1</sup>—which include  $\text{B}_4\text{C}$ ,  $\text{B}_6\text{O}$ ,  $\text{B}_6\text{P}$ ,  $\text{B}_6\text{S}$ ,  $\text{B}_6\text{As}$ ,  $\text{B}_{13}\text{N}_2$ ,  $\text{B}_6\text{Se}$ , and  $\text{SiB}_3$ .<sup>2–6</sup> Besides a high thermal stability, these materials possess a low mass density, extreme hardness, chemical inertness, and variable semiconductor properties.<sup>7–10</sup>  $\alpha\text{-B}_{12}$ -derived solids have been intensively investigated not only for their useful materials properties but also for their unusual structures and “electron-deficient” chemical bonding.<sup>11–13</sup> The majority of compounds have homogeneity ranges, especially with respect to the nonboron component.<sup>2,3</sup> This work deals with the representative  $\text{SiB}_3$ , which, as we will outline below, assumes a special role.

The most essential features of  $\alpha\text{-B}_{12}$ -derived materials are summarized in Figure 1. In the  $\alpha\text{-B}_{12}$  structure (space group  $R\bar{3}m$ , shown in Figure 1a,b),  $\text{B}_{12}$  icosahedra are oriented with their threefold rotational axis along the body diagonal of the rhombohedral unit cell (or along the  $c$  axis when referring to hexagonal axes) and arranged as in a cubic close packing (ccp).<sup>14</sup>

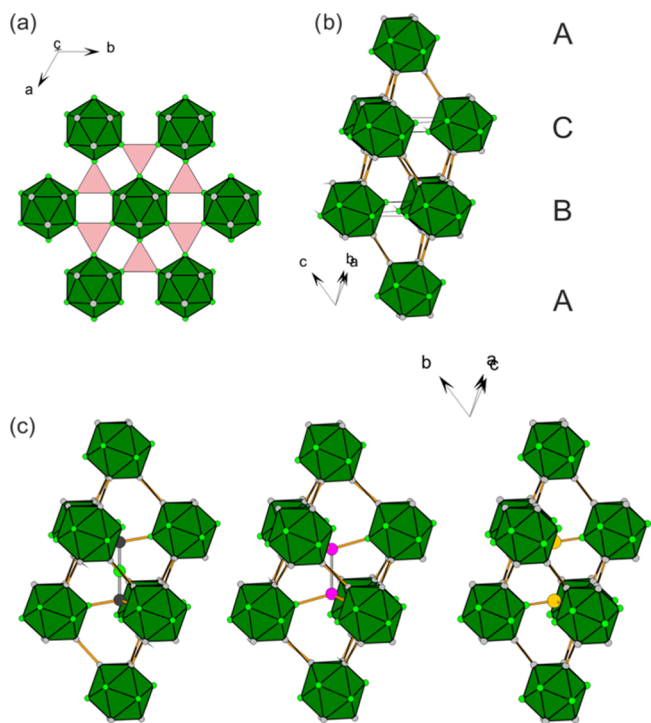


**Figure 1.** Crystal structure of rhombohedral  $\alpha\text{-B}_{12}$  and its (major) “icosahedral boron-rich” derivatives. In the  $\alpha\text{-B}_{12}$  structure, icosahedral  $\text{B}_{12}$  units are arranged as in a cubic close packing. (a) Arrangement of  $\text{B}_{12}$  units within a close-packed layer. Intralayer 3c2e bonds involving equatorial B atoms are indicated as pink triangles. (b) Rhombohedral unit cell of  $\alpha\text{-B}_{12}$  with stacking of layers indicated. Terminal (exo) 2c2e bonds connecting icosahedra between layers are depicted as yellow lines. (c) In the binary/ternary derivatives, interlayer 3c2e bonds are replaced by terminal 2c2e bonds to interstitial atoms. From left to right:  $\text{B}_4\text{C}$  ( $[\text{B}_{11}\text{C}^{\text{P}}]^-[\text{CBC}]^+$ ),  $\text{B}_6\text{P}$  ( $[\text{B}_{12}]^{2-}[\text{P}_2]^{2+}$ ),  $\text{B}_6\text{O}$  ( $[\text{B}_{12}]^{2-}[\text{O}^+]_2$ ). The center of the interstitial atoms corresponds to the location of the octahedral void in the cubic close packing.

Boron atoms occupy two sites which are distinguished as polar,  $\text{B}^{\text{P}}$ , and equatorial,  $\text{B}^{\text{e}}$ . The former are situated on opposite triangles along the threefold direction, whereas equatorial ones form a puckered hexagon ring (i.e., represent the “waist” of icosahedra). The bonding situation of  $\alpha\text{-B}_{12}$  is easily rationalized by employing established electron-counting schemes.<sup>15–18</sup> Between close-packed layers, neighboring icosahedra are connected via terminal (exo) bonds involving two  $\text{B}^{\text{P}}$  atoms, whereas within-layers icosahedra are linked via 3c2e bonds involving the  $\text{B}^{\text{e}}$  atoms. The different bonding motifs ( $\text{B}_{12}$  skeleton, terminal 2c2e, and intralayer 3c2e) are well reflected in the distribution of involved B–B interatomic distances: those range from 1.75 to 1.81 Å for skeleton bonded atoms within clusters and are 1.67 and 2.01 Å for 2c2e and 3c2e connected atoms, respectively.<sup>14</sup>

The structures of  $\alpha\text{-B}_{12}$ -derived icosahedral boron-rich solids arise when inserting three-atom chains CBC or NBN (leading to  $\text{B}_4\text{C}$ <sup>19</sup> and  $\text{B}_{13}\text{N}_2$ ,<sup>20</sup> respectively) or pairs of atoms (dumbbells) at the position of the octahedral voids in the ccp arrangement of icosahedra, and orienting them along  $[111]_h/[001]_h$  (Figure 1c).<sup>2,3</sup> This replaces the intralayer 3c2e bonds between  $\text{B}^{\text{e}}$  atoms by 2c2e exo-links between  $\text{B}^{\text{e}}$  and an atom of the inserted entity, whereas the exo-links between  $\text{B}^{\text{P}}$  atoms of neighboring icosahedra between layers are retained. Substitution of B atoms within  $\text{B}_{12}$  units occurs rarely and is mostly seen with boron carbides, where it affects the polar position.  $\text{B}_4\text{C}$  may be written as  $\text{CBC}(\text{B}_{11}\text{C}^{\text{P}})^{\text{P}}$ .<sup>21</sup> Optimum electron counts for the various materials (yielding electron-precise semiconducting phases) follow from the optimum electron count of an all exo-linked icosahedral cluster (i.e., 13 electron pairs for skeleton bonding and 12 electrons for exo-bonding),<sup>15,18</sup> which may be expressed as, e.g.,  $(\text{CBC})^+(\text{B}_{11}\text{C}^{\text{P}})^-$ ,  $(\text{P}_2)^{2+}\text{B}_{12}^{2-}$ , and  $(\text{O}^+)_2\text{B}_{12}^{2-}$  (cf. Figure 1c). However, as initially mentioned,  $\alpha\text{-B}_{12}$ -derived materials are rarely stoichiometric with respect to the electron-precise composition. Compositional deviations frequently originate from disorder within the three-atom/dumbbell entities, according to  $\text{B}_{12}(\text{B}_{1-x}\text{X}_x)$  for, e.g., X = P, S, Se or  $\text{B}_{12}\text{Y}_{2-x}$  for, e.g., Y = As, P, O,<sup>2,3</sup> in addition to the above-mentioned substitution of  $\text{B}^{\text{P}}$  by  $\text{C}^{\text{P}}$ . Although phase relations may be complicated, homogeneity ranges remain rather narrow and semiconductor properties are maintained.<sup>3,22</sup>

$\text{SiB}_3$  represents a special case among  $\alpha\text{-B}_{12}$ -derived materials. Although rhombohedral  $\text{SiB}_3$  has been known for a long time—first reports date back to Moissan and Stock<sup>23</sup>—its composition is still discussed controversially and will be hereafter referred to as  $\text{SiB}_{3-x}$ . In contrast to  $\text{B}_4\text{C}$ , the larger size of Si permits only the presence of Si dumbbells in the octahedral voids. This is analogous to  $\text{B}_6\text{P}$ <sup>4</sup>—but in contrast to  $\text{B}_6\text{P}$  (Figure 1c), an electron-precise composition (conforming to a semiconductor phase) will require the substitution of a substantial concentration of B within icosahedra. Early single-crystal diffraction work indicated that the preferred location for this substitution is, as for  $\text{B}_4\text{C}$ , the polar site.<sup>24</sup> The electron-precise composition  $\text{Si}_2(\text{B}_{10}\text{Si}^{\text{P}}_2)$ , i.e.,  $\text{SiB}_{2.5}$ , however, does not seem to be realized. Thus, in contrast to other  $\alpha\text{-B}_{12}$ -derived materials,  $\text{SiB}_{3-x}$  attains a composition that deviates considerably from the optimum electron count and, accordingly, this phase should be truly metallic. Obviously, substitution of Si for boron atoms on the polar site implies highly strained icosahedra. This follows simply

from a comparison of atomic radii, which are rather similar for B and C (0.82 and 0.77 Å, respectively), whereas there is a large disparity in size with respect to the third period element Si (1.11 Å).<sup>25</sup> As seen in the molecular analogues, such strained icosahedra are clearly unfavorable: There are numerous derivatives of icosahedral dicarboranes ( $C_2B_{10}H_{12}$ ), where H can be substituted for, e.g., alkyl, acyl, or halogens. Icosahedral dicarboranes exist in all three isomers (ortho, meta, para) and the  $C_2B_{10}$  skeleton may be stable up to 600 °C.<sup>26</sup> In contrast, icosahedral disilaboranes are only known as air-sensitive 1,2-diphenyl-, 1,2-methylphenyl-, and 1,2-dimethyl-*ortho*-disilaborane.<sup>27</sup> The latter,  $(CH_3)_2Si_2B_{10}H_{10}$ , was discovered first.<sup>28</sup> The actual composition of  $SiB_{3-x}$  will represent a balance of the two extremes  $SiB_{2.5}$  (electron-precise with all bonding states occupied but highly strained  $B_{10}Si^P_2$  icosahedra) and  $SiB_6$  (partially empty valence band but unstrained  $B_{12}$  icosahedra). In this context, it is interesting to note that recently a new boron carbide phase  $B_{2.5}C$  was predicted, which is more stable than  $B_4C$  at high-pressure conditions.<sup>29</sup> The structure of  $B_{2.5}C$  corresponds to electron-precise  $C_2(B_{10}C^P_2)$ . Furthermore, it has been suggested that microalloying  $B_4C$  with silicon—where CBC units are (partially) replaced by  $Si_2$  dumbbells—could afford a ternary material with decisively improved ductility.<sup>30</sup> And it has been shown that also hypothetical  $Si_2(B_{10}Si^P_2)$  displays improved ductility with respect to  $B_4C$ .<sup>31</sup>

Apart from its uncertain composition, also formation conditions and the thermal stability of  $SiB_{3-x}$  are poorly understood. It seems to be clear that above 1300 °C,  $SiB_{3-x}$  decomposes to orthorhombic  $SiB_6$  and  $Si$ <sup>32,33</sup> and recent phase diagrams specify 1270 °C as the peritectoid decomposition temperature.<sup>34–36</sup> However, the decomposition of  $SiB_{3-x}$  has also been reported at temperatures below 1250 °C,<sup>37</sup> whereas at the same time, significant rates of formation would require temperatures above 1250 °C.<sup>38</sup> Further, single crystals of  $SiB_{3-x}$  used in structural studies were obtained from Si-rich melts for which temperatures had to exceed 1400 °C.<sup>24</sup> Aselage then put forward the interesting proposal that  $SiB_{3-x}$  is merely metastable, which could indeed explain the seemingly contradictory reports on synthesis conditions and thermal stability.<sup>39</sup> To this day, the thermodynamic properties of rhombohedral  $SiB_{3-x}$  have remained nebulous. Also,  $SiB_{3-x}$  lacks conclusive characterization of its physical properties.

It then came as a surprise when in 2003 Salvador et al. reported a strictly ordered and stoichiometric phase  $SiB_3$ , which they termed  $\beta$ - $SiB_3$  (and subsequently, rhombohedral  $SiB_3$  was named  $\alpha$ - $SiB_3$ ).<sup>40</sup>  $\beta$ - $SiB_3$  was obtained from a metal (Ga) flux synthesis at comparatively low synthesis temperatures (850–1000 °C). The orthorhombic crystal structure of  $\beta$ - $SiB_3$ , shown in Figure 2, consists of layers of interconnected  $B_{12}$  icosahedra parallel to the *ac* plane, which are stacked, but not bonded, in the *b* direction. Linear zigzag chains of  $Si_4$  rhomboid rings are embedded between these layers. Each  $Si_4$  ring connects to eight  $B_{12}$  units and, as a consequence, each Si atom attains a peculiar fivefold coordination by three Si and two B atoms. All B atoms in an icosahedron attain an exo-bond, either to B atoms of neighboring icosahedra in the *ac* plane or to Si atoms of neighboring  $Si_4$  rings. The bonding properties of  $\beta$ - $SiB_3$  have been qualitatively rationalized by assigning each (all-exo-bonded)  $B_{12}$  unit a charge of -2 and, accordingly, each rhomboid ring  $Si_4$  a charge of +2.<sup>41</sup> Bonding in nonclassical  $Si_4^{2+}$  was then described by a simple 4c4e model.<sup>41–43</sup> According to this bonding model,  $\beta$ - $SiB_3$  is electron-precise, which is in agreement with its semiconductor properties (i.e., a band gap of

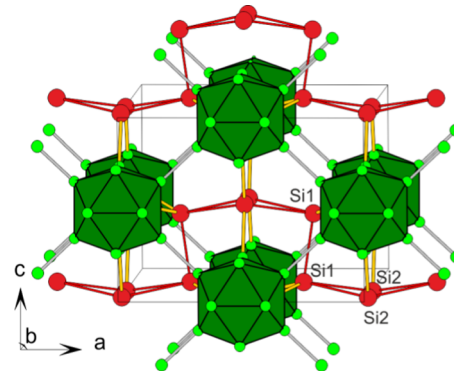


**Figure 2.** Crystal structure of orthorhombic  $\beta$ - $SiB_3$ . B and Si atoms are depicted as green and red circles, respectively. Zigzag chains of rhomboid  $Si_4$  rings are indicated by red bonds. Terminal 2c2e (exo) bonds between icosahedra and between B and Si atoms are drawn in gray and yellow, respectively.

2 eV).<sup>40</sup> Thus, the structural properties of  $\beta$ - $SiB_3$ , and presumably also the physical and electronic ones, are radically different from  $\alpha$ - $SiB_{3-x}$ .

Salvador et al. argued that a liquid Ga environment was necessary to stabilize  $\beta$ - $SiB_3$ , which apparently is not accessible by conventional synthetic routes (as used for the synthesis of  $\alpha$ - $SiB_{3-x}$ ).<sup>40</sup> Later studies showed that also liquid In and Sn environments promote the formation of  $\beta$ - $SiB_3$ ,<sup>44</sup> and it was proposed that to obtain  $\beta$ - $SiB_3$ , the formation of  $\alpha$ - $SiB_{3-x}$  had to be completely bypassed.<sup>45</sup> Generally, metal fluxes may allow for kinetic control in the synthesis of solids<sup>45</sup> and/or access to low-temperature modifications for which rates of formation can be insignificant when using solid reactants. Thus, one may suspect that  $\beta$ - $SiB_3$  represents a metastable and/or low-temperature form of  $SiB_3$ . However, a transition from  $\beta$ - $SiB_3$  to  $\alpha$ - $SiB_{3-x}$  has never been observed. Instead,  $\beta$ - $SiB_3$  has been shown to be extraordinarily temperature-stable (refractory).<sup>40</sup> So, how does then  $\beta$ - $SiB_3$  (thermodynamically) relate to  $\alpha$ - $SiB_{3-x}$ , and—given the long history of B–Si investigations—why has it not been observed earlier? In this work, we establish the formation conditions for both  $\alpha$ - $SiB_{3-x}$  and  $\beta$ - $SiB_3$  from binary elemental mixtures. We further bracket the composition of  $\alpha$ - $SiB_{3-x}$  and show that this phase is metastable with respect to  $\beta$ - $SiB_3$  at high temperatures.

## 2. METHODS

**2.1. Synthesis.** Unless otherwise stated, starting materials for synthesis were amorphous boron (95–97%, ABCR GmbH (AB114S07), <1 μm average particle size), silicon powder with an average particle size 8 μm (99.995%, ABCR GmbH, in the following, we denote this material as “micron-Si”), and silicon powder with an average particle size <50 nm (98%, Alfa Aesar; in the following, we denote this material as “nano-Si”). Before use, micron-Si was ground in an agate mortar, after which the particle size distribution was 1–5 μm. Boron was treated overnight in dynamic vacuum ( $10^{-4}$ – $10^{-5}$  mbar) at 900 °C. All precursors were stored and handled for sample preparation in an Ar-filled glovebox. BN crucibles [8.5 mm outside diameter (OD), 6.5 mm inside diameter (ID), 10 mm height] or boron nitride powder (98%, Sigma-Aldrich), both used for confining reaction mixtures, were also degassed in a dynamic vacuum before use. Niobium ampoules (10 mm OD, 9 mm ID, about 50 mm length) were cleaned with dilute HCl and acetone before use.

**2.1.1. Synthesis of Polycrystalline Samples.** For a typical synthesis, boron and silicon starting material were intimately but gently mixed in an agate mortar, avoiding grinding. Considered molar proportions Si/B ranged from 1:1 to 1:4. Mixtures were subsequently pressed into pellets with 4 or 6 mm diameter. For this, the highest pressure tolerable with the pressing tool was applied (~250 MPa). The height of a pellet was between 1 and 1.5 mm, the weight of 4 mm pellets was around 15 mg, and that of 6 mm pellets about 40 mg. It is important to mention that reproducible results could only be obtained with well-pressed and homogeneously dense pellets and using starting materials from the same batch. One or several pellets were placed in a BN crucible, which in turn was inserted in a niobium ampule. Alternatively, a Nb ampule was filled with slightly compacted BN powder into which Si–B pellets were embedded. Nb ampules were sealed shut by arc welding, removed from the glovebox, and then placed in a high-temperature furnace, in which they were heated in an Ar atmosphere. Target temperatures were in a range of 1100–1300 °C, and dwelling times varied from several hours to several days, up to 2 weeks. The typically applied heating rate was 200 °C/h. After dwelling, the samples were cooled by switching off the furnace. To achieve complete and precise control of the sample/reaction temperature, systematic investigations were performed in a Netzsch STA 449 F1 Jupiter thermal analysis apparatus using a thermogravimetric analysis sample rod. For this, 4 mm pellets of reaction mixture were placed in polycrystalline sapphire crucibles (5 mm ID, 6 mm OD, 5 mm height) from CoorsTek, which were covered with a thin corundum lid. Heating ramps were 10 °C/min. All Jupiter experiments were performed using a continuous Ar gas flow (5 N, 85 mL/min) and in the presence of an oxygen getter (Zr metal). Pellets were broken into pieces after sintering, which were either ground for powder X-ray diffraction (PXRD) or used for scanning electron microscopy analysis.

**2.1.2. Synthesis of  $\alpha\text{-SiB}_{3-x}$  Single-Crystal Samples.** Boron and silicon starting material were intimately mixed in a molar proportion Si/B = 10:1, and the mixture was pressed into pellets (6 mm diameter, height 2–3 mm). Several pellets (batch size, 0.5–2.0 g) were placed in a BN crucible/embedded in BN powder and then sealed in a Nb ampule. Batch sizes amounted between 0.5 and 2.0 g. Nb ampules were placed in a high-temperature furnace and heated in Ar atmosphere at a rate of 200 °C/h to 1435 °C, which is slightly above the melting point of Si (1414 °C). After equilibrating the sample at this temperature for 1 h, the furnace was turned off and the ampule was cooled to room temperature. Subsequently, the ampule was cut open and the Si–B ingot was recovered and cleaned from the surrounding BN (if present). The ingot was crushed into coarse pieces (about 1–2 mm), and excess Si was removed with a mixture of deionized water, concentrated  $\text{HNO}_3$ , and concentrated HF (volume proportions, 3:2:2). The remainder consisted mostly of black  $\alpha\text{-SiB}_{3-x}$  crystals, with sizes between several  $\mu\text{m}$  to several hundred  $\mu\text{m}$ . The acid mixture was decanted and the crystals washed with water (3×) and ethanol. The crystals were subsequently used for single-crystal X-ray diffraction, scanning electron microscopy (SEM), and Raman spectroscopy investigations.

**2.1.3. Synthesis at High Pressures.** High-pressure syntheses were performed in a 6–8 Walker-type multi-anvil high-pressure device using an 18/12 assembly developed by Stoyanov et al.<sup>46</sup> Powders of crystalline  $\beta$ -boron (99.95%, ChemPur) and silicon (99.999%, Sigma-Aldrich) were mixed with molar ratios Si/B = 1:2 and 1:3 and placed inside hexagonal boron nitride capsules

in an Ar-filled glovebox. The total amount of starting materials mixture varied between 65 and 120 mg. To prepare the high-pressure cell assembly, BN sample capsules were positioned in a graphite furnace, which in turn was placed together with a zirconia thermal insulating sleeve (0.57 mm wall thickness, 7.77 mm OD, 10.80 mm length) in a magnesia octahedron with 18 mm edge length. Sample capsules were pressurized at a rate of about 0.5 GPa/h with 25 mm Toshiba grade E tungsten carbide cubes truncated to 12 mm edge length. After reaching the target pressure (either 5.5 or 8 GPa), the samples were heated to a target temperature between 900 and 1200 °C within an hour. The temperature was monitored by a type-C thermocouple (W5%Re–W26%Re) close to the sample. After applying the dwelling time, the samples were quenched by turning off the power to the furnace (quench rate ~50 °C/min and at approximately constant pressure). Afterward, the pressure was released at a rate of approximately 0.5 GPa/h. The recovered, cylindrically shaped, sample was crushed and coarsely ground. Excess Si was removed by treating the ground samples twice with hot NaOH solution (20%, 6 h with stirring) and then with HCl and aqua regia. This procedure yielded crystalline  $\text{SiB}_3$  samples with <5 wt % elemental Si impurity.

**2.2. Powder X-ray Diffraction (PXRD) Analysis.** PXRD patterns were collected on two PANalytical X’Pert PRO diffractometers, using  $\text{Cu K}\alpha_1$  and  $\text{Cu K}\alpha$  radiation, respectively, at room temperature and in reflection mode. Powder samples were spread onto zero-background Si plates, and the patterns were recorded in  $2\theta$ , with a step size of about 0.015° for patterns used for phase analysis and about 0.007° for patterns used for Rietveld refinements. Phase/weight fractions were estimated roughly using the HighScore Plus v3.0e software from Panalytical B.V., together with data from the ICDD PDF-4+ v4.18.0.2 database, or determined more accurately using the Rietveld method through the program package FULLPROF.<sup>47</sup> Typically, the Rietveld refinements proceeded by first modeling the background by linear interpolation using a set of refinable height background points, refining unit cell parameters, and sample displacement together with scale factors, and then fitting Bragg reflection profiles by a pseudo-Voigt function (number 7 in FullProf). Employed structure models were taken from the ICSD database;  $\alpha\text{-SiB}_{3-x}$  (space group  $\overline{R}\bar{3}m$ , ICSD no. 28317, ref 24),  $\beta\text{-SiB}_3$  (space group  $Imma$ , ICSD no. 412621, ref 40), and  $\text{SiB}_6$  (space group  $Pnmm$ , ICSD no. 63554, ref 48). For  $\alpha\text{-SiB}_{3-x}$ , an  $hkl$ -dependent broadening with broadening vector [010] significantly improved the fit. For  $\beta\text{-SiB}_3$ , a preferred orientation along [010] was modeled with the March–Dollase function.<sup>49</sup>

**2.3. Scanning Electron Microscopy (SEM) Investigations.** SEM investigations comprised morphological and compositional analysis [by energy-dispersive X-ray (EDX) spectroscopy] of sintered pellet and crystal samples. In addition, the morphology and particle size distribution of the starting materials was examined (Figures S16 and S18, Supporting Information). For studying sintered pellets, a piece of sample was affixed to an Al holder with melting glue (mp 150 °C) and conducting graphite paste was added to ensure electric conduction from sample to holder. Polishing was first done mechanically with SiC paper to create a flat surface, which was followed by  $\text{Ar}^+$ -beam cross section polishing (CP) in a CP-09010 instrument from JEOL. CP was performed at a 90° angle, employing a shield from the manufacturer, and using 5.5 kV acceleration voltage for the  $\text{Ar}^+$ -ion gun. For studying crystal samples, crystals were selected under an optical microscope and

placed on the flat surface of an Al sample holder using a droplet of acetone to affix the crystals.

All SEM investigations were performed in an SEM JSM-7000F from JEOL that is equipped with an l-N<sub>2</sub> cooled Inca energy-dispersive detector from Oxford Instruments. For EDX analysis, a low acceleration voltage of 5 kV was employed to decrease the characteristic X-ray generation volume and thereby receive better resolution and more reliable EDX data from the low Z elements (i.e., boron) in the sample. Images were generated using information from secondary electrons or backscattered electrons at a working distance of 15 mm and at a medium high probe current setting (7 in the instrument settings). EDX probing was performed at a work distance of 10 mm with a high probe current setting (14 in the instrument settings). The specific difficulties in obtaining quantitative analysis of Si/B ratios with EDX are discussed in the *Supporting Information*.

#### 2.4. Single-Crystal X-ray Diffraction (SC-XRD) Analysis.

**2.4.1. Data Collection.** The detailed SC-XRD analysis described in Section 3.2.1 refers to a single crystal with dimensions 0.125 × 0.137 × 0.155 mm<sup>3</sup>, which was mounted on a micro-loop using perfluorinated polyalkylether. Data were collected on a Bruker SMART diffractometer using a microfocus X-ray source ( $\lambda = 0.56087 \text{ \AA}$ ) equipped with mirror-optics and an APEXII charge-coupled device (CCD) detector at room temperature. To resolve the disorder of the structure, data of high resolution and high quality are needed. Intensity data were therefore collected using a total of 14  $\omega$ -scans with 360/600 frames per scan and a frame width of 0.5/0.3°. The lower frame width was only used for the maximum 2θ offset. The detector distance was 4 cm, and the detector offsets were 2θ = 0° (6x), 2θ = 34° (3x), and 2θ = 68° (5x). A wide range of exposure times between 3 and 135 s had to be employed, mainly due to the rapid decay of scattering intensity with increasing scattering angle.

**2.4.2. Data Reduction.** Crystal data for  $\alpha\text{-SiB}_{3-x}$  (SiB<sub>2.64(2)</sub>):  $M_r = 54.45$ ,  $a = 6.3282(1) \text{ \AA}$ ,  $c = 12.7283(3) \text{ \AA}$ ,  $V = 441.43(2) \text{ \AA}^3$ ; trigonal space group R3m (#166);  $Z = 12$ ;  $F(000) = 314.0$ ;  $\rho_{\text{calc}} = 2.458 \text{ g/cm}^3$ ;  $\mu(\text{Ag K}\alpha) = 0.44 \text{ mm}^{-1}$ . The frames were integrated with the Bruker SAINT<sup>50</sup> V8.34A software package using the narrow-frame algorithm, and the unit cell was determined from a total of 9923 reflections. A multiscan absorption correction ( $T_{\min} = 0.91$  and  $T_{\max} = 0.95$ ) as well as the interframe scaling and an error model was then applied using SADABS v2014/2.<sup>51</sup> The internal agreement factor was  $R_{\text{int}} = 0.0363$  for a total of 27 377 reflections (1311 unique). The data set provided a completeness of 99.54% ( $|h| \leq 17$ ,  $|k| \leq 17$ ,  $|l| \leq 35$ ) and a redundancy of 20.9 for the complete data  $6.38^\circ < \theta < 105.16^\circ$  ( $d_{\min} = 0.353 \text{ \AA}$ ,  $\sin(\theta_{\max})/\lambda < 1.416 \text{ \AA}^{-1}$ ). Subsequent refinements were performed with the program package JANA2006.<sup>52</sup>

**2.5. Spectroscopic Investigations.** **2.5.1. Raman Spectroscopy.** Raman spectra on  $\alpha\text{-B}_{12}$ ,  $\alpha\text{-SiB}_{3-x}$ , and  $\beta\text{-SiB}_3$  crystals were measured using a LabRAM HR 800 spectrometer equipped with an 800 mm focal length spectrograph and an air-cooled, back-thinned CCD detector. The spatial resolution of the instrument is specified as  $\sim 1 \mu\text{m}$ . The crystal samples were placed on a glass slide and excited with a double-frequency Nd:YAG laser (532 nm). Spectra were collected at room temperature with an exposure time of 300 s and using a grating of 1800 lines/mm. For disordered  $\alpha\text{-SiB}_{3-x}$ , the laser power was varied from very low to very high. This did not lead to any notable changes in the spectra. All spectra were calibrated and normalized.  $\alpha\text{-B}_{12}$  was synthesized from crystalline  $\beta$ -boron in a

Pt-flux at 5.5 GPa and 1000 °C using a 6–8 Walker-type multi-anvil high-pressure device (see Section 2.1 for details). The dwell time was 15 min.

#### 2.5.2. Magic Angle Spinning (MAS) NMR Spectroscopy.

The <sup>29</sup>Si MAS NMR spectrum of a powder sample containing  $\alpha\text{-SiB}_{3-x}$  and nonreacted Si was acquired on a Bruker Avance III 600 spectrometer operating at a magnetic field of 14.1 T (119.22 MHz <sup>29</sup>Si Larmor frequency), with a 4 mm HXY probe. The acquisition was carried out at 12 kHz MAS using a single radio frequency (rf) excitation pulse of 1.4  $\mu\text{s}$  and 60 Hz nutation frequency, corresponding to a  $\sim 30^\circ$  flip angle. A total of 160 signal transients with a 600 s recycle delay were collected. Neat tetramethylsilane was used for chemical shift referencing and rf power calibration.

#### 2.6. Computational Investigations.

**2.6.1. First-Principles Calculations.** Total energies of  $\alpha\text{-SiB}_{3-x}$  ( $x = 0.5, 0.18, 0, -0.2, -0.67$ ) and  $\beta\text{-SiB}_3$  and of the elemental phases  $\alpha\text{-B}_{12}$  and  $\alpha\text{-Si}$ , were calculated within the density functional theory (DFT)<sup>53,54</sup> and the projector augmented wave method,<sup>55</sup> as implemented in the Vienna Ab initio Simulation Package (VASP).<sup>56,57</sup> The generalized gradient approximation, developed by Perdew, Burke, and Ernzerhof,<sup>58</sup> was employed to account for electron exchange–correlation effects. The energy cutoff for plane waves, included in the expansion of wave functions, was set to 500 eV, and a  $9 \times 9 \times 9$  Monkhorst–Pack  $k$ -point mesh<sup>59</sup> was chosen for the Brillouin zone integration. The calculated total energies were converged within an accuracy of 1 meV/atom with respect to both the energy cutoff and the number of  $k$ -points. During structural optimizations, all atomic coordinates, volume, and cell shape of the considered phases were allowed to be relaxed. To derive the total electronic density of states (DOS), the tetrahedron method for the Brillouin zone integration was employed.<sup>60</sup>

**2.6.2. Cluster Expansion (CE) of  $\alpha\text{-SiB}_{3-x}$ .** To search for the energetically stable composition and relevant atomic configurations of disordered  $\alpha\text{-SiB}_{3-x}$ , the cluster expansion (CE) method was employed. According to the CE formalism,<sup>61</sup> the total energy ( $E$ ) of any crystalline solid that is strictly a function of the atomic arrangement on a lattice [i.e., a so-called atomic configuration ( $\sigma$ )] can be formally expanded into a sum over correlation functions  $\zeta_f^{(n)}(\sigma)$  of specific  $n$ -site figures  $f$  with the corresponding effective cluster interactions (ECIs)  $V_f^{(n)}$

$$E(\sigma) = N \sum_f m_f^{(n)} V_f^{(n)} \zeta_f^{(n)}(\sigma) \quad (1)$$

The factor  $m_f^{(n)}$  is defined as the multiplicity of specific  $n$ -site figures  $f$ , normalized to the number of atom sites  $N$  within the corresponding atomic configuration  $\sigma$ . To describe any atom configuration  $\sigma$  of  $\alpha\text{-SiB}_{3-x}$ , the spin variable  $\sigma_i$  is assigned to take on a value of +1 or of −1, if the lattice site  $i$  is occupied by a B or by a Si atom, respectively. As a result, any atomic configuration  $\sigma$  of  $\alpha\text{-SiB}_{3-x}$  can be uniquely specified by a set of spin variables  $\{\sigma_i\}$ , and the correlation function  $\zeta_f^{(n)}$  can subsequently be determined by the products of the spin variables  $\sigma_i$

$$\zeta_f^{(n)} = 1/m_f^{(n)} \sum_{\alpha} \left( \prod_{i \in \alpha} \sigma_i \right) \quad (2)$$

where the sum of the products in the parentheses runs over all symmetrically equivalent clusters,  $\alpha \in f$ . Although the expansion, expressed in eq 1, is analytically exact in the limit of inclusion of all possible figures  $f$ , it must be truncated for practical purposes.

To perform the CE, the MIT Ab initio Phase Stability (MAPS) code,<sup>62</sup> as implemented in the alloy-theoretical automated toolkit,<sup>63</sup> was used to truncate the expansion in eq 1 and to determine the ECIs in such a way that eq 1 returns the total energies  $E(\sigma)$  of  $\alpha\text{-SiB}_{3-x}$  as close to those obtained from first-principles calculations as possible for all  $\sigma$  included in the expansion. In the present investigation, the CE method was employed to determine the ground-state atomic configurations of  $\alpha\text{-SiB}_{3-x}$  of different compositions, in particular  $\alpha\text{-SiB}_{2.5}$  and  $\alpha\text{-SiB}_3$ . Because of strong experimental evidence,<sup>24</sup> only atoms on the polar site were considered in the CE.

**2.6.3. Phonon Calculations.** The total and partial phonon density of states (pDOS) of  $\beta\text{-SiB}_3$  and of the most stable configurations of  $\alpha\text{-SiB}_{2.5}$  (as derived from the CE method) were obtained at the level of the harmonic approximation using the finite-displacement method, as implemented in the PHONOPY package for phonon calculations.<sup>64,65</sup> Force constants were calculated within  $2 \times 2 \times 2$  orthorhombic (triclinic) primitive unit cells using the Parlinski–Li–Kawazoe method with an atomic displacement of  $0.01 \text{ \AA}$ .<sup>66</sup> To ensure the convergence of the phonon calculations, the supercells of  $\alpha\text{-SiB}_{2.5}$  and  $\beta\text{-SiB}_3$  were fully relaxed so that the total forces acting on each atom within the supercells were less than  $10^{-6} \text{ eV/\AA}$ . A  $35 \times 35 \times 35$  Monkhorst–Pack  $k$ -point grid was used to sample the supercells for deriving the phonon frequencies and vibrational free energy as a function of temperature.

### 3. RESULTS AND DISCUSSION

**3.1. Synthesis of SiB<sub>3</sub>: Interplay between  $\alpha\text{-SiB}_{3-x}$  and  $\beta\text{-SiB}_3$ .** The initial preparation of a compound SiB<sub>3</sub> was reported in 1900,<sup>23</sup> but could not be repeated until 1959–1962, during which several publications on silicon borides SiB<sub>3</sub> and SiB<sub>4</sub><sup>32,37,38,67–70</sup> appeared. These, and all later reports on rhombohedral SiB<sub>3</sub> and SiB<sub>4</sub>, refer to the same phase, i.e.,  $\alpha\text{-SiB}_{3-x}$ . Knarr<sup>32</sup> and Brosset and Magnusson<sup>37</sup> found that mixtures of silicon and boron heated between 1200 and 1380 °C first produced  $\alpha\text{-SiB}_{3-x}$ , which then slowly decomposed into orthorhombic SiB<sub>6</sub> plus Si. At the same time, pure samples of  $\alpha\text{-SiB}_{3-x}$ , or mixtures of  $\alpha\text{-SiB}_{3-x}$  and SiB<sub>6</sub>, appeared unchanged after annealing at 1260 °C.<sup>32</sup>  $\alpha\text{-SiB}_{3-x}$  has been assumed to undergo a peritectoid (solid state) decomposition (into SiB<sub>6</sub> and Si) at temperatures between 1270<sup>32</sup> and 1340 °C.<sup>71</sup> Most recent Si–B phase diagrams specify 1270 °C as the decomposition temperature (and assign a very narrow homogeneity range to  $\alpha\text{-SiB}_{3-x}$ ,  $x \approx 0.1$ ).<sup>34–36</sup> With respect to the synthesis of  $\alpha\text{-SiB}_{3-x}$ , Colton reported that the rates of both formation and subsequent decomposition increase as temperature increased from 1250 to 1350 °C.<sup>38</sup> Later, Tremblay and Angers derived “optimum” synthesis conditions: Rates of formation and decomposition appeared to be balanced best for  $T = 1325 \text{ }^\circ\text{C}$  and  $t = 5.75 \text{ h}$  (referring to synthesis mixtures B/Si = 3.5).<sup>72</sup>

An important step was the crystal structure determination of  $\alpha\text{-SiB}_{3-x}$  by Magnusson and Brosset (MB),<sup>24</sup> which revealed (i) the close relationship of  $\alpha\text{-SiB}_{3-x}$  to rhombohedral B<sub>4</sub>C and B<sub>6</sub>P and (ii) a rather Si-rich composition, i.e., SiB<sub>2.89</sub>. Interestingly, the single crystals used for the structural study were prepared from molten silicon–boron mixtures, i.e., at temperatures above 1400 °C. In 1998, Aselage summarized splendidly the state of affairs and arrived at the conclusion that  $\alpha\text{-SiB}_{3-x}$  is actually not thermodynamically stable. Instead, its formation is kinetically driven and  $\alpha\text{-SiB}_{3-x}$  would form only under conditions of boron supersaturation of a silicon-rich solid or liquid solution.<sup>39</sup> The salient question is whether Aselage’s insightful analysis is

compatible with, or how it possibly connects to, the later discovery of  $\beta\text{-SiB}_3$  from molten metal flux synthesis. In the following, we describe our attempts to uncover the interplay between  $\alpha\text{-SiB}_{3-x}$  and  $\beta\text{-SiB}_3$  in the binary Si–B system by applying different synthesis strategies.

Reproducible results for the synthesis of SiB<sub>3</sub> from mixtures of elemental boron and silicon required tightly pressed and homogeneously dense pellets as well as precise control of the sample temperature. Therefore, we performed investigations into reaction temperatures and times in the well-controlled environment of a thermal analysis apparatus. Figure 3 shows results for mixtures of nano-Si and amorphous boron with ratios 1:3 and 1:4, which were reacted at temperatures between 1150 and 1225 °C.

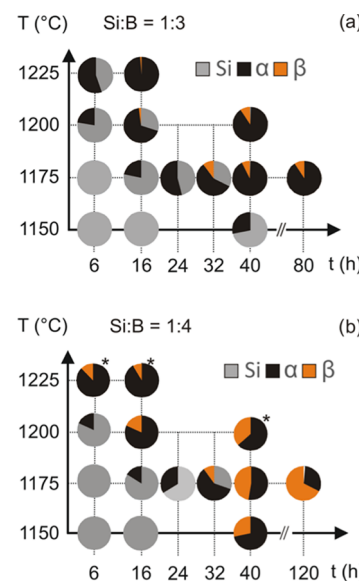


**Figure 3.** Summary of the synthesis results using nano-Si and amorphous boron as starting materials with Si/B ratios 1:3 (a) and 1:4 (b). The relative fractions of unreacted Si,  $\alpha\text{-SiB}_{3-x}$ , and  $\beta\text{-SiB}_3$  are presented as pie charts. The asterisks mark the presence of SiB<sub>6</sub> phase in products.

Focusing first on the 1:3 reaction mixtures (Figure 3a), rates of formation are very low at 1150 °C. No silicon boride products were observed after 6 and 16 h. However, it was notable that amorphous boron started converting into crystalline  $\beta$ -boron with some Si incorporated (i.e., SiB<sub>36</sub>).<sup>73</sup> This conversion was also observed for pure amorphous boron starting material in a control experiment (see Figure S17, Supporting Information). After 40 h, about 25% of Si had reacted with  $\alpha\text{-SiB}_{3-x}$ . At 1175 °C, rates appeared significantly increased. Already after 16 h, the product contained about 25%  $\alpha\text{-SiB}_{3-x}$  and after 40 h, virtually all Si had been consumed. The 40 h product corresponded to ~90%  $\alpha\text{-SiB}_{3-x}$  and, surprisingly, ~10%  $\beta\text{-SiB}_3$ . The product mixture after 80 h showed a slightly increased fraction of  $\beta\text{-SiB}_3$ . At 1200 °C, reaction rates were increased again significantly. After 6 and 16 h, a 25 and 70% conversion to  $\alpha\text{-SiB}_{3-x}$  was obtained, respectively. The product after 40 h was essentially the same as that obtained at 1175 °C after 40 h. Reactions at 1225 °C resulted in more than 50% conversion after 6 h and an essentially phase-pure  $\alpha\text{-SiB}_{3-x}$  sample after 16 h. The PXRD pattern of this sample has subsequently been used for Rietveld refinement of  $\alpha\text{-SiB}_{3-x}$  (cf. Figure 8, see later discussion). The 40 h experiment produced largely SiB<sub>6</sub>.

For 1:4 reaction mixtures (Figure 3b), we observed an increased reaction rate compared to 1:3 mixtures. Complete consumption of Si was observed at 1225 °C after only 6 h, at 1200 °C after 16 h, and at 1150 °C after 40 h. At the same time, it is clear that excess B promotes the formation of  $\beta$ -SiB<sub>3</sub>, which was obtained in substantial amounts (25–50%) at 1150–1200 °C after 40 h. Figure 4 illustrates with PXRD patterns the evolution of the product with time at 1175 °C. We observed significant formation of SiB<sub>6</sub> at 1225 °C after 16 h.

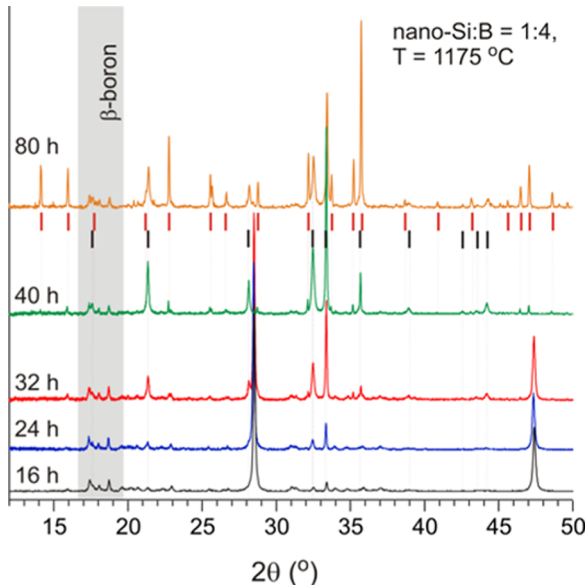


**Figure 4.** PXRD patterns (Cu K $\alpha_1$  radiation) of products from Si/B 1:4 reaction mixtures after dwelling at 1175 °C for various times (cf. Figure 3b). The position of diffraction lines for  $\alpha$ -SiB<sub>3-x</sub> and  $\beta$ -SiB<sub>3</sub> is indicated by the black and red markers, respectively. The 2 $\theta$  range containing pronounced reflections from SiB<sub>6</sub> ( $\beta$ -boron structure) is marked in gray.

We summarize the results from the nano-Si/amorphous boron reactions as follows:  $\alpha$ -SiB<sub>3-x</sub> formation takes place already at 1150 °C, although at low rate. Comparatively small increases of  $T$  give large effects on the rate of formation. At temperatures above 1200 °C, the formation of SiB<sub>6</sub> was observed, which is in agreement with earlier reports.<sup>32,37</sup> Importantly,  $\beta$ -SiB<sub>3</sub> can be obtained from binary reactions mixtures and was consistently seen after 40 h reaction time. We mention briefly the results obtained from micron-Si/amorphous boron and nano-Si/crystalline boron reactions (details can be found in Supporting Information Figures S1–S9). Increasing the particle size of Si reduced the rate of  $\alpha$ -SiB<sub>3-x</sub> formation, whereas the usage of crystalline boron seemed to increase rates. This perhaps unexpected finding may relate to the sluggish onset of reactions with nano-Si/amorphous mixtures at 1150 and 1175 °C, during which amorphous boron partially crystallized before SiB<sub>3-x</sub> formation was observed (after 40 and 16 h, respectively).

We confirmed the earlier observed relative ease of formation of  $\alpha$ -SiB<sub>3-x</sub>. It appears that the particle size of Si is an important parameter in this respect, as reactions with nano-Si could be performed at unprecedentedly low temperatures (1150 °C). Using nano-Si, we find that the optimum  $T,t$  conditions for achieving roentgenographically pure samples of  $\alpha$ -SiB<sub>3-x</sub> is sintering at 1225 °C for 16 h (referring to tightly pressed pellets with ratio 1:3 of the starting materials specified). We also

mention that it is possible to exploit the comparatively fast kinetics of  $\alpha$ -SiB<sub>3-x</sub> formation for the simultaneous synthesis and consolidation of  $\alpha$ -SiB<sub>3-x</sub> specimens in a spark plasma sintering device and refer for further details to Supporting Information (Figure S12).

According to Aselage, the reaction of silicon and boron (to yield  $\alpha$ -SiB<sub>3-x</sub>) proceeds by the following sequence. First, boron diffuses into silicon, ultimately reaching saturation. (Note that boron diffuses rapidly in Si<sup>74,75</sup> but the solubility of B in Si is very low, 0.2% at 1000 °C.<sup>34–36</sup>) Second, under conditions of boron supersaturation,  $\alpha$ -SiB<sub>3-x</sub> nucleates and begins to grow. This hypothesis is supported by our finding that the particle size of Si has a large effect on the reaction rate. Figure 5a shows the

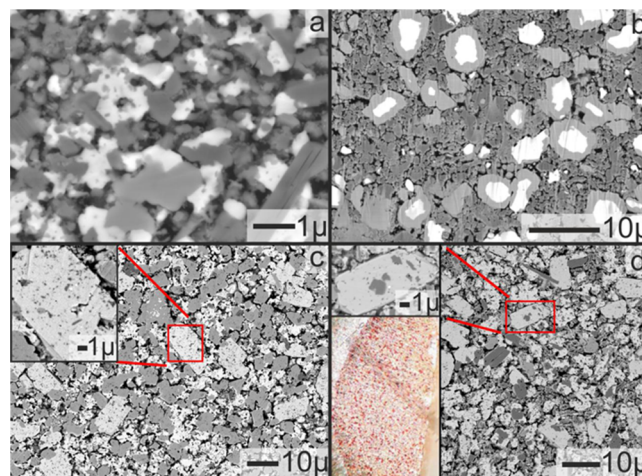


**Figure 5.** SEM backscattered electron images of reacted pellets revealing various stages of  $\alpha$ -SiB<sub>3-x</sub>/ $\beta$ -SiB<sub>3</sub> formation. For a homogenously dense sample, areas with bright and dark contrast correspond to Si- and B-rich compositions, respectively. (a) Nano-Si/B = 1:4 at 1175 °C after 16 h: onset of  $\alpha$ -SiB<sub>3-x</sub> formation. White, dark, and medium gray areas correspond to agglomerated nano-Si, crystallized amorphous boron, and irregularly shaped, wormlike,  $\alpha$ -SiB<sub>3-x</sub> particles, respectively. (b) Micron-Si/B = 1:4 at 1200 °C after 24 h: Si particles with a B-saturated rim and irregularly shaped, wormlike,  $\alpha$ -SiB<sub>3-x</sub> particles. (c) Nano-Si/B = 1:3 at 1200 °C after 40 h: roentgenographically pure  $\alpha$ -SiB<sub>3-x</sub> sample, consisting of larger crystals (brighter) and smaller particles (darker). Areas in between  $\alpha$ -SiB<sub>3-x</sub> crystals and particles appear darker due to a lower sample density. (d) Nano-Si/B = 1:4 at 1175 °C after 40 h: the sample constitutes  $\beta$ -SiB<sub>3</sub> crystals, irregularly shaped  $\alpha$ -SiB<sub>3-x</sub> particles, and crystallized excess boron (dark gray areas). The smaller inset shows a  $\beta$ -SiB<sub>3</sub> crystal with boron-rich inclusions; the larger inset shows an optical micrograph of the cross section polished sample. The reddish  $\beta$ -SiB<sub>3</sub> crystals are clearly visible.

SEM image of a nano-Si/B = 1:4 pellet after sintering at 1175 °C for 16 h, and Figure 5b shows a micron-Si/B = 1:4 pellet after sintering at 1200 °C for 24 h. In the former sample, nano-Si appears to be agglomerated to larger, 0.1–1  $\mu$ m, particles and amorphous boron partially crystallized to SiB<sub>6</sub> ( $\beta$ -boron) crystals with sizes of several micrometers (in agreement with the PXRD pattern, cf. Figure 4).  $\alpha$ -SiB<sub>3</sub>, which according to PXRD is present at a 20% level (with respect to Si, cf. Figure 3b), is seen as rather irregular (“wormlike”) particles with sizes around 1  $\mu$ m. The SEM image of the latter sample shows clearly Si particles with their original size (1–5  $\mu$ m) and shape and possessing a boron-enriched rim. This rim may be envisioned to develop and host  $\alpha$ -SiB<sub>3-x</sub> nuclei, which subsequently grow to wormlike

crystallites. Upon growth,  $\alpha\text{-SiB}_{3-x}$  crystallites detach from the surface of a Si particle, which eventually gets consumed.

**Figure 5c** shows the SEM image of a nano-Si/B = 1:3 pellet after sintering at 1200 °C for 40 h. According to PXRD (**Figure 3a**), this sample corresponded to almost pure  $\alpha\text{-SiB}_{3-x}$ . At these conditions,  $\alpha\text{-SiB}_{3-x}$  was afforded as faceted crystals with sizes of up to 10  $\mu\text{m}$ . At the same time, one can note more irregularly shaped crystals with a smaller size. Interestingly, their different contrast suggests a different composition, with the larger crystals more rich in Si (i.e., larger crystals appear brighter in the micrograph). A closer look at the larger crystals reveals heterogeneities in the presence of boron-rich inclusions and sporadic Si nanocrystals. We infer that the crystal growth of  $\alpha\text{-SiB}_{3-x}$  is accompanied with a change to a more Si-rich composition. This is corroborated by single-crystal diffraction studies and discussed in more detail in **Section 3.2**. It is not clear whether sizable (>10  $\mu\text{m}$ ) homogeneous  $\alpha\text{-SiB}_{3-x}$  crystals can be grown in solid-state reaction mixtures. On the other hand, Magnusson and Brosset discovered that  $\alpha\text{-SiB}_{3-x}$  crystals can be grown in Si–B melts using excess of Si,<sup>24,37</sup> i.e., at temperatures considerably above the decomposition into  $\text{SiB}_6$  and Si. Here, one can think that—analogous to  $\alpha\text{-SiB}_{3-x}$  formation from boron-supersaturated Si particles in the solid state— $\alpha\text{-SiB}_{3-x}$  nuclei precipitate from boron-supersaturated Si-rich liquid solutions by following Ostwald's rule of stages (which postulates that a supersaturated system does not spontaneously transform into the most stable of all possible states (i.e.,  $\text{SiB}_6 + \text{Si}$ ) but rather into the state which is the next more stable compared to the supersaturated state). In our synthesis of  $\alpha\text{-SiB}_{3-x}$  crystal samples (according to Magnusson and Brosset), we used a Si/B ratio close to the eutectic composition (~92 atom % of Si) and heated to temperatures just slightly above the eutectic temperature (~1385 °C).<sup>34–36</sup> Melts were equilibrated for a relatively short time (1 h), to minimize decomposition into  $\text{SiB}_6$ , after which the sample was cooled by switching off the furnace. After removal of excess Si, black  $\alpha\text{-SiB}_{3-x}$  crystals were obtained with sizes from several micrometers to 200  $\mu\text{m}$  (see **Figure 6**).

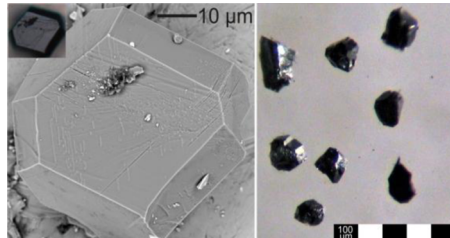


**Figure 6.** View of  $\alpha\text{-SiB}_{3-x}$  crystals. Left: SEM and optical microscopy image (inset) of a selected crystal. Right: optical microscopy image of a selection of crystals with sizes around 100  $\mu\text{m}$ .

Sintered reaction pellets and  $\alpha\text{-SiB}_{3-x}$  crystals were subjected to extensive EDX analysis (see **Figures S13–S15**, Supporting Information). Flux-grown crystals showed homogeneous values, 25(1) atom % Si and 75(1) atom % B, within and between crystal specimens, which indicates a composition near  $\text{SiB}_3$ , i.e.,  $x \approx 0$ . However, as discussed in **Section 2.3**, Si/B ratios obtained from EDX cannot be considered accurate due to lack of standards. EDX analysis of sintered pellets was in addition hampered by the small size and irregular shape of particles. Backscattered electron images, as shown in **Figure 5**, provide qualitative information on Si/B compositional variations. At the same time, one has to be aware of the fact that because of the

heterogeneous nature of sintered reaction pellets, contrast variations will also be caused by density differences between sample areas (cf. **Figure 5c**).

The oversight of  $\beta\text{-SiB}_3$  as product from binary reaction mixtures in earlier works is surprising since we could consistently obtain it irrespective of the choice of Si starting material (nano or micro) or Si/B ratio (1:3 or 1:4). Most likely,  $\beta\text{-SiB}_3$  escaped previous investigations because of the comparatively low temperatures and long reaction times needed. The evolution of products from nano-Si/B = 1:4 reaction mixtures at 1175 °C strongly suggests that  $\beta\text{-SiB}_3$  forms from conversion of  $\alpha\text{-SiB}_{3-x}$ , which is greatly assisted by the presence of excess B. Accordingly, the reaction  $\alpha\text{-SiB}_{3-x} + x\text{B} = \beta\text{-SiB}_3$  is comparatively fast, whereas the direct conversion  $3/(3-x)\alpha\text{-SiB}_{3-x} = \beta\text{-SiB}_3 + x\text{Si}$ , which is assumed to occur in 1:3 reaction mixtures, is slow. Importantly, both conversions occur in a narrow temperature window, 1175–1200 °C. Nano-Si/B = 1:4 reactions afforded  $\beta\text{-SiB}_3$  as 5–10  $\mu\text{m}$  sized crystallites, which could be easily noted by their characteristic orange-red color upon inspecting samples in an optical microscope.

**Figure 5d** shows the SEM image of a nano-Si/B = 1:4 pellet after sintering at 1175 °C for 40 h. According to PXRD, this sample consisted of approximately equal proportions  $\alpha\text{-SiB}_{3-x}$  and  $\beta\text{-SiB}_3$ .  $\beta\text{-SiB}_3$  crystallites, embedded in a matrix of irregularly shaped  $\alpha\text{-SiB}_{3-x}$  particles, can be recognized by their sharp edges. (Note that the growth of  $\alpha\text{-SiB}_{3-x}$  single crystals is not expected at 1175 °C as this requires temperatures of 1200 °C and above.) Most of the  $\beta\text{-SiB}_3$  crystals actually contain B-rich inclusions, which may be attributed to a heterogeneous nature of the  $\alpha$ -to- $\beta$  conversion. Prolonged (several days to weeks) annealing experiments using Si-rich Si/B mixtures with ratios 1:2 and 1:1 also produced  $\beta\text{-SiB}_3$  crystals (see **Figures 7** and **S10**). Therefore, it has to be assumed that  $\beta$ -

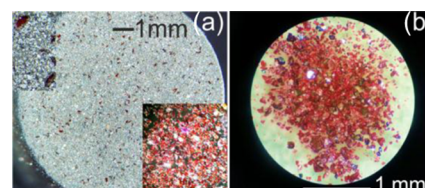


**Figure 7.** Various views of  $\beta\text{-SiB}_3$  samples. (a) Image of a micron-Si/B = 1:2 pellet after sintering for 2 weeks at 1200 °C. The diameter of the pellet is 5 mm. The inset at the top left shows close-up, highlighting orange, faceted,  $\beta\text{-SiB}_3$  crystals protruding from the pellet surface. The lower inset shows the remainder of the pellet after dissolution of excess Si with a mixture  $\text{H}_2\text{O}/\text{HF}/\text{HNO}_3$ . (b)  $\beta\text{-SiB}_3$  sample obtained from high-pressure synthesis (8 GPa, 1100 °C) using a close to stoichiometric mixture of crystalline boron and micron-Si (after crushing and washing the sample with hot 20% NaOH solution).

$\text{SiB}_3$  is a thermodynamically stable binary compound in the Si–Bi system. We observed that pure  $\beta\text{-SiB}_3$  samples convert to a mixture of  $\text{SiB}_6$  and Si in a temperature interval 1250–1300 °C. The peritectoid decomposition is slow and cannot be recognized in a differential thermal analysis/differential scanning calorimetry (DSC) experiment. Similarly, and as already noted by Knarr,<sup>32</sup> pure samples of  $\alpha\text{-SiB}_{3-x}$  appear stable up to 1250–1300 °C (**Figure S11**, Supporting Information).

Salvador et al. showed that the kinetic barriers associated with  $\beta\text{-SiB}_3$  formation can be overcome by the application of a molten metal flux.<sup>40</sup> Alternatively, the application of high pressures should minimize barriers associated with diffusion and thus

allow the synthesis of  $\beta$ -SiB<sub>3</sub> at much shorter times and lower temperatures. This was then confirmed in experiments where Si/B reaction mixtures were compressed to 5.5–8 GPa and subsequently heated.  $\alpha$ -SiB<sub>3</sub> formed quantitatively after 6 h at the lowest dwelling temperature applied, 900 °C. Quantitative  $\beta$ -SiB<sub>3</sub> formation, presumably through  $\alpha$ -to- $\beta$  conversion, was obtained at 1100 °C within 12 h. At 1300 °C, the product constituted a mixture of SiB<sub>6</sub> and Si.

To conclude this section, we report more detailed results from the PXRD analyses of the various samples. Figure 8 shows

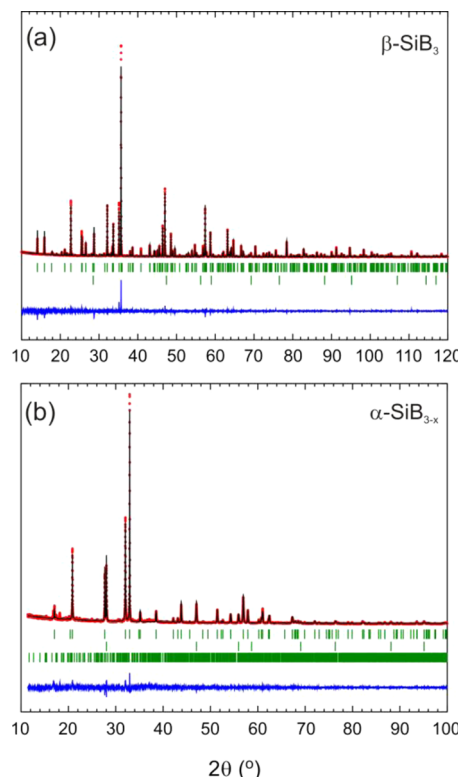


**Figure 8.** Rietveld fit to PXRD patterns (Cu K $\alpha$  radiation) of  $\beta$ -SiB<sub>3</sub> (obtained from reaction pellets micron-Si/B = 1:2 which were annealed at 1200 °C for 2 weeks) (a) and  $\alpha$ -SiB<sub>3-x</sub> (as obtained from a reaction pellet nano-Si/B = 1:3 after sintering at 1250 °C for 16 h) (b). See Tables 1 and 2 for the refinement results. Secondary phases included in the refinements are Si (a, b) and SiB<sub>6</sub> (b).

Rietveld fits to PXRD patterns of samples of  $\beta$ -SiB<sub>3</sub> (Figure 8a) and  $\alpha$ -SiB<sub>3-x</sub> (Figure 8b), and Tables 1 and 2 compile the results of the refinements. The obtained structure parameters for  $\beta$ -SiB<sub>3</sub> agree well with the initially reported model of Salvador et al. (based on single-crystal X-ray diffraction data)—and there is no reason to doubt the established crystal structure of  $\beta$ -SiB<sub>3</sub>. Intensities in the PXRD pattern of the  $\alpha$ -SiB<sub>3-x</sub> sample decrease rapidly with increasing  $2\theta$ , which is characteristic for disordered materials. At first sight, the fit to the structure model of Magnusson and Brosset appears reasonable. The refined occupancy of the polar icosahedral position (~33% Si) suggests a composition, which is close to the electron-precise composition SiB<sub>2.5</sub>. However, site occupancies from PXRD data will not be reliable because of the lack of intensity for high-angle reflections. For the same reason, the refined  $U_{iso}$  values are 3–4 times larger compared to  $\beta$ -SiB<sub>3</sub>, whose PXRD pattern displays more regular intensities for the high-angle reflections. It is interesting to note that the molar volumes of  $\alpha$ -SiB<sub>3-x</sub> and  $\beta$ -

**Table 1.** Crystallographic Data and Structure Refinement for  $\alpha$ -SiB<sub>3-x</sub> and  $\beta$ -SiB<sub>3</sub> from PXRD Measurements

compound	$\beta$ -SiB <sub>3</sub>	$\alpha$ -SiB <sub>3-x</sub>
space group	Imma (74)	R $\bar{3}m$ (166)
crystal system	orthorhombic	trigonal
<i>a</i> (Å)	8.3902(2)	6.3394(3)
<i>b</i> (Å)	12.5641(3)	
<i>c</i> (Å)	6.2133(1)	12.7464(3)
<i>V</i> (Å <sup>3</sup> )	654.97(3)	443.62(1)
$\rho$ (g/cm <sup>3</sup> )	2.455	2.478
$R_F$ (%)	5.25	5.45
$R_p$ (%)	6.72	8.87
$R_{wp}$ (%)	8.82	11.0
$R_{exp}$ (%)	3.29	5.58
$\chi^2$	7.18	3.91
number of points	16 564	16 564
number of fitted parameters	38	28
number of independent reflections	288	105

SiB<sub>3</sub> are very similar, which implies that  $\beta$ -SiB<sub>3</sub> is not a high-pressure phase in the Si–B system. Table 3 reports the refined lattice parameters of  $\alpha$ -SiB<sub>3-x</sub> as obtained from the various synthesis experiments. There are slight variations, possibly indicating a slightly variable Si/B ratio for polycrystalline  $\alpha$ -SiB<sub>3-x</sub> samples consisting of micron-sized particles.

As a result of our synthesis efforts, we could clarify the interplay between  $\alpha$ -SiB<sub>3-x</sub> and  $\beta$ -SiB<sub>3</sub> in the binary B–Si system.  $\alpha$ -SiB<sub>3-x</sub> appears metastable, whereas  $\beta$ -SiB<sub>3</sub> represents a stable phase in the B–Si phase diagram. Both compounds decompose between 1250 and 1300 °C into SiB<sub>6</sub> and Si. In the next section, we address the precise composition and detailed structural properties of disordered  $\alpha$ -SiB<sub>3-x</sub>.

**3.2. Structural and Compositional Characterization of  $\alpha$ -SiB<sub>3-x</sub>.** Although the structure and composition of  $\beta$ -SiB<sub>3</sub> is firmly established from single-crystal X-ray diffraction studies,<sup>40</sup> the same does not hold true for  $\alpha$ -SiB<sub>3-x</sub>. The early structural investigations by Magnusson and Brosset in 1962<sup>24</sup> were based on diffraction data recorded on a Weissenberg camera. Modern single-crystal diffraction methods allow for vastly superior data and also provide tools for the analysis of disordered structures. It is important to note that the refinement of Si–B mixed occupancies from high-resolution data represents a rather accurate composition analysis for single crystals since the form factors for Si and B are sufficiently but not extremely different. For polycrystalline bulk samples, we will show that <sup>29</sup>Si MAS NMR spectroscopy provides the most reliable method for compositional analysis.

**3.2.1. SC-XRD Investigation.** High-resolution SC-XRD data were collected from several  $\alpha$ -SiB<sub>3-x</sub> crystals. Particular attention was paid to the possible presence of superstructure reflections, indicating long-range correlation of disorder. However, we could not detect superstructure reflections for any of the investigated crystals. For the initial independent atom refinement, we employed the structure model of Magnusson and Brosset (MB), which assumes the polar icosahedral position as mixed B/Si site and a single isotropic atomic displacement parameter (ADP) for all atoms ( $U_{iso} = 0.0143 \text{ \AA}^2$ ). Due to the high resolution of our data, individual and anisotropic ADPs could be introduced immediately. The position and ADP of the mixed site was constrained to be equal, and the sum of occupancies was constrained to unity. The obtained atom position parameters agreed reasonably with the MB results. The

**Table 2.** Fractional Atomic Coordinates and Isotropic Displacement Parameters for  $\alpha\text{-SiB}_{3-x}$  and  $\beta\text{-SiB}_3$  from PXRD Measurements

atom	site	<i>x/a</i>	<i>y/b</i>	<i>z/c</i>	$U_{\text{iso}}$ ( $\text{\AA}^2$ )	s.o.f.
$\beta\text{-SiB}_3, Imma$						
Si1	8i	0.2697(4)	0.25	0.0643(5)	0.0147(8)	
Si2	8h	0	0.3458(1)	-0.0033(5)	0.0146(6)	
B1	16j	0.3914(9)	0.3886(3)	-0.001(1)	0.016(1)	
B2	8h	0	0.4239(6)	0.270(2)	0.024(2)	
B3	8h	0	0.4255(6)	-0.277(2)	0.019(2)	
B4	16j	0.176(1)	0.4989(5)	-0.344(1)	0.015(1)	
$\alpha\text{-SiB}_{3-x} R\bar{3}m$						
B1	18h	0.156(2)	-0.156(2)	0.025(1)	0.046(7)	
B2	18h	0.112(1)	-0.112(1)	0.882(1)	0.056(6)	0.66(2)
Si1	18h	0.112(1)	-0.112(1)	0.882(1)	0.056(6)	0.34
Si2	6c	0	0	0.4045(9)	0.038(4)	

**Table 3.** Compilation of Lattice Parameters for  $\alpha\text{-SiB}_{3-x}$  Obtained from Various Reactions<sup>a</sup>

reactions	<i>a</i> ( $\text{\AA}$ )	<i>c</i> ( $\text{\AA}$ )	<i>V</i> ( $\text{\AA}^3$ )	phase fraction
1:2.6, 1240 °C, 24 h (NMR)	6.341	12.745	443.9	72.2
1:3, 1225 °C, 16 h (Rietveld)	6.339	12.746	443.6	98.2
1:2, 1175 °C, 24 h	6.342	12.752	444.1	
1:2, 1250 °C, 24 h	6.339	12.749	443.7	
1:3, 1200 °C, 24 h	6.340	12.748	443.7	93.7
1:3, 1200 °C, 24 h	6.341	12.749	443.9	23.0
1:3, 1250 °C, 24 h	6.338	12.745	443.3	
1:3, 1250 °C, 24 h	6.339	12.747	443.6	93.7
1:4, 1175 °C, 24 h	6.339	12.745	443.5	
1:4, 1250 °C, 24 h	6.338	12.745	443.3	
nano 1:3, 1175 °C, 16 h	6.341	12.749	443.9	89.6
nano 1:3, 1200 °C, 40 h	6.341	12.749	443.9	39.2
nano 1:4, 1175 °C, 40 h	6.336	12.739	442.9	57.0
nano 1:4, 1175 °C, 80 h	6.341	12.749	443.9	45.5
nano 1:4, 1175 °C, 120 h	6.349	12.750	444.0	17.0
nano 1:4, 1225 °C, 6 h	6.337	12.743	443.2	93.0
average	6.340	12.747	443.7	
max-min	0.006	0.013	1.2	

<sup>a</sup>Estimated standard deviations are below 0.001 for the lattice parameters and 0.1 for the volumes.

occupancy of the mixed site, 32.4(6)% Si, corresponds to a composition  $\text{SiB}_{2.55(3)}$ , which is significantly lower than the result of MB (i.e.,  $\text{SiB}_{2.89}$ ) and only slightly larger than the ideal, electron-precise stoichiometry of  $\text{SiB}_{2.5}$  with two Si atoms per icosahedron. However, the MB model is intrinsically flawed with respect to its interatomic distances. For example, the length of the exo-bond connecting two icosahedra via polar atoms is 1.632(2)  $\text{\AA}$ , which is actually shorter than the  $\text{B}^{\text{P}}\text{-B}^{\text{P}}$  exo-distance in the  $\alpha\text{-B}_{12}$  structure, and thus far too short to also account for a Si–B exo-bond. In addition, the refinement only converged at a modest *R*-value of  $R_1 = 10.1\%$ . The residual electron density ranged from -4.5 to 10.2  $\text{e}/\text{\AA}^3$ . The maximum in residual electron density (positive *Q*-peak) was located inside the icosahedron at a distance of approximately 0.42  $\text{\AA}$  to the mixed occupied polar site.

In the next step, the constraint of equal position was removed and the boron atom slightly pushed inward the icosahedron, to provide some bias for the least-squares routine. The refinement improved with lower  $R_1$  and  $\Delta\rho$  (see model 1 in Table 4). The distance between  $\text{B}^{\text{P}}$  and  $\text{Si}^{\text{P}}$  atoms at the polar position was 0.38  $\text{\AA}$ , which compared very well with the original distance of the *Q*-

**Table 4.** Evolution of *R* Values, Residual Density Maxima (Full Resolution), and Refined Composition upon Improving the Structural Model for  $\alpha\text{-SiB}_{3-x}$  in the Refinement of SC-XRD Data.

model	$R_1$ (%)	$\Delta\rho$ ( $\text{e}/\text{\AA}^3$ )	refined composition
MB	10.15	+10.25/-4.41	$\text{SiB}_{2.55(3)}$
1 (split-position)	6.50	+3.05/-4.99	$\text{SiB}_{2.00(1)}$
2 (individual-ADP)	2.74	+1.52/-1.14	$\text{SiB}_{2.58(1)}$
3 (split- $\text{B}_\text{P}$ )	2.30	+1.42/-0.36	$\text{SiB}_{2.61(2)}$
4 (anharmonic)	1.98	+0.55/-0.35	$\text{SiB}_{2.64(2)}$

peak. Although exo-distances of 1.98  $\text{\AA}$  between  $\text{B}^{\text{P}}$  and  $\text{Si}^{\text{P}}$  atoms are reasonable, this model has a different shortcoming: The site occupancy for  $\text{Si}^{\text{P}}$  increased to 44%, which translates to an unreasonable composition  $\text{SiB}_{2.00(1)}$ . A large and negative *Q*-peak of -4.99  $\text{e}/\text{\AA}^3$  on the  $\text{B}^{\text{P}}$  atom clearly indicated the flawed occupancy of this model.

The crucial hint on how to improve became evident when removing the constraint of equal ADPs between  $\text{Si}^{\text{P}}$  and  $\text{B}^{\text{P}}$  atoms (model 2). The resulting  $R_1$  and  $\Delta\rho$  values were again reduced significantly and the composition swung back to  $\text{SiB}_{2.58(1)}$ . The split  $\text{B}^{\text{P}}\text{-Si}^{\text{P}}$  distance decreased to 0.28  $\text{\AA}$  and the ADP of the  $\text{B}^{\text{P}}$  atom almost doubled ( $U_{\text{eq}} = 0.019 \text{\AA}^2$ ) and became strongly prolate, with the long axis pointing toward the  $\text{Si}^{\text{P}}$  atom. The largest negative *Q*-peak of -1.14  $\text{e}/\text{\AA}^3$  is now located inside the icosahedron close to the  $\text{B}^{\text{P}}$  atom. This  $\text{B}^{\text{P}}$  position is now conveniently split into two individual boron positions  $\text{B}^{\text{P},\text{Si}}$  and  $\text{B}^{\text{P},\text{B}}$  (model 3) after which the negative *Q*-peak disappeared, along with a further reduced  $R_1$ . (The notation  $\text{B}^{\text{P},\text{A}}$  has been chosen to indicate that the boron atom shows a reasonable exo-distance with respect to an atom A in the neighboring icosahedron.) Note that the ADP for these split boron atoms was kept equal for stability reasons and the sum of the occupancies for  $\text{B}^{\text{P},\text{Si}}$ ,  $\text{B}^{\text{P},\text{B}}$ , and  $\text{Si}^{\text{P}}$  was constrained to unity.

The disorder at the polar positions is expected to lead to slight perturbations of the ordered  $\text{B}^{\text{e}}$  and  $\text{Si}^{\text{d}}$  (dumbbell) atoms, which result in deviations from the harmonic probability density distribution. In fact, the largest *Q*-peaks were mainly located close to the  $\text{Si}^{\text{d}}$  positions, in particular, above and below the Si dumbbells. In the final step, we therefore added up to third order ( $\text{B}^{\text{P}}$ ) and up to fourth order ( $\text{Si}^{\text{d}}$ ) Gram–Charlier anharmonic ADPs<sup>76</sup> (model 4), which was also justified by non-negative probability distribution maps (see Figure S20, Supporting Information). The refinement of 39 parameters against 1181 reflections [ $F_{\text{o}} > 3\sigma(F_{\text{o}})$ ,  $\sin(\theta_{\text{max}})/\lambda < 1.416 \text{\AA}^{-1}$ ] finally

**Table 5.** Fractional Coordinates, Equivalent Isotropic ADP Values  $U_{\text{eq}}$ , and Site Occupancy Factors for  $\alpha\text{-SiB}_{3-x}$  Model 4 [Space Group  $R\bar{3}m$ ,  $a = 6.3282(1)$ ,  $c = 12.7283(3)$ ]

atom	site	$x/a$	$y/b$	$z/c$	$U_{\text{eq}} (\text{\AA}^2)$	s.o.f.
B <sup>e</sup>	18h	0.15673(6)	0.31345(12)	0.02634(7)	0.01142(6)	1.0
B <sup>p,B</sup>	18h	0.1124(3)	-0.1124(3)	0.8849(3)	0.0092(2)	0.374(4)
B <sup>p,Sn</sup>	18h	0.0932(2)	-0.0932(2)	0.9009(2)	0.0092(2)	0.319(4)
Si <sup>p</sup>	18h	0.1138(1)	0.1138(1)	0.87447(8)	0.0115(1)	0.308(1)
Si <sup>d</sup>	6c	0	0	0.40518(3)	0.00678(7)	1.0

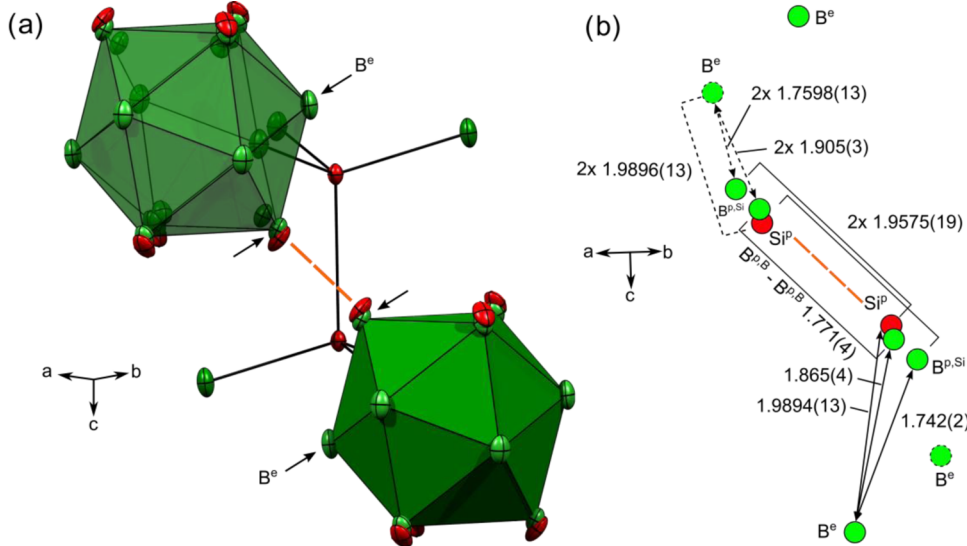


**Figure 9.** (a) Structural fragment of  $\alpha\text{-SiB}_{3-x}$  model 4, as determined by SC-XRD; Si and B atoms are shown in red and green, respectively. Thermal ellipsoids are drawn at the 50% probability level. Coordination polyhedra are drawn transparent and nontransparent and connect only to  $\text{B}^{\text{p},\text{B}}$  atoms at the disordered site. (b) Projection of the exo-bond (dashed orange line) onto the plane defined by arrows in (a). Note that the dashed black lines and dashed atoms are out of plane.

converged at  $R_1 = 1.98\%$ ,  $wR_1 = 3.08\%$ , and a featureless residual density distribution of  $\Delta\rho = +0.34/-0.27 \text{ e}/\text{\AA}^3 [\sin(\theta)/\lambda < 1.0 \text{ \AA}^{-1}]$ . Table 5 lists the atom position parameters for model 4. Anharmonic ADP values are given as Tables S1 and S2, Supporting Information. For supporting crystallographic data, see ref 77.

In the following, we discuss model 4, which is depicted in Figure 9, in more detail. The polar position is split into three sites, a Si position ( $\text{Si}^{\text{p}}$ ) and two boron positions ( $\text{B}^{\text{p},\text{Sn}}$  and  $\text{B}^{\text{p},\text{B}}$ ). Their refined occupancies are  $\text{Si}^{\text{p}}$ : 30.8(1)%;  $\text{B}^{\text{p},\text{Sn}}$ : 31.9(4)% and  $\text{B}^{\text{p},\text{B}}$ : 37.4(4)%, which yields the composition  $\text{SiB}_{2.64(2)}$  for the crystal. Model 4 accounts well for the various interatomic distances in the disordered structure (see Figure 9b and Table 6). Exo-bonds between polar atoms may occur between  $\text{Si}^{\text{p}}$  and  $\text{B}^{\text{p},\text{Sn}}$  atoms,  $d = 1.958(2) \text{ \AA}$ , as well as between two  $\text{B}^{\text{p},\text{B}}$  atoms,  $d = 1.771(4) \text{ \AA}$ . Note that only a  $\text{Si}^{\text{p}}-\text{B}^{\text{p},\text{Sn}}$  contact yields a meaningful Si–B interatomic distance and, therefore, one expects an equal—or very similar—contribution of these atoms to the polar site. This is indeed the case for model 4. Furthermore, the occupation of the  $\text{Si}^{\text{p}}$  site is below 1/3, which also supports the model since short  $\text{Si}^{\text{p}}-\text{Si}^{\text{p}}$  contacts can be avoided. The implication of model 4 is that reasonable distances are provided for all combinations [polar–polar–exo, polar–polar–skeleton, polar–equatorial–(skeleton)] upon Si incorporation into the polar position (cf. Table 6).

The validity of model 4 is further supported by analyzing data of several more crystals. In all cases, the refined occupancies were not significantly different. The composition  $\text{SiB}_{2.64(2)}$  suggests the presence of 88%  $\text{B}_{10}\text{Si}^{\text{p}}_2$  and 12%  $\text{B}_{11}\text{Si}^{\text{p}}$  icosahedra

in the disordered  $\alpha\text{-SiB}_{3-x}$  structure (the occurrence of  $\text{B}_{12}$  or  $\text{B}_9\text{Si}^{\text{p}}_3$  icosahedra is rather unlikely; see next section). As a reminder, 100%  $\text{Si}_2\text{B}_{10}$  and 100%  $\text{SiB}_{11}$  icosahedra would correspond to the compositions  $\text{SiB}_{2.5}$  and  $\text{SiB}_{3.67}$ , respectively.

**3.2.2.  $^{29}\text{Si}$  MAS NMR Spectroscopy.** The refined occupancy of several crystals suggests a narrow range of composition for  $\alpha\text{-SiB}_{3-x}$   $\text{SiB}_{2.62}-\text{SiB}_{2.64}$ , i.e., around 27.5 atom % Si. This value is more accurate than the one obtained from EDX analysis of  $\alpha\text{-SiB}_{3-x}$  crystals [25(1) atom % Si]. SEM investigations (cf. Figure 5c) indicated that  $\alpha\text{-SiB}_{3-x}$  single crystals possess a higher Si content than the small, micrometer-sized, particles that initially form in a solid-state bulk synthesis.

To also obtain clarity about the composition of  $\alpha\text{-SiB}_{3-x}$  bulk samples, we performed a  $^{29}\text{Si}$  MAS NMR measurement of a sample that also contained a larger fraction unreacted nano-Si (about 20%). The  $^{29}\text{Si}$  MAS NMR spectrum of this sample, shown in Figure 10, revealed three distinct resonances. The signal with peak maximum at -104 ppm is attributed to unreacted Si, in agreement with ref 78. The signals with peak maxima at 11 and -64 ppm are assigned to Si atoms in the polar icosahedral and dumbbell positions, respectively. With this assignment, the tetrahedrally coordinated dumbbell Si attains a chemical shift that is closer to that of the elemental structure, whereas the six-coordinated Si appears more deshielded because its electrons contribute to delocalized icosahedral bonding, which in turn would result in a positively polarized nature. Both signals are relatively broad, due to the  $^{29}\text{Si}$  chemical shifts distribution as a consequence of the disorder. The width of the

**Table 6. Interatomic Distances in Model 4 (Estimated Standard Deviations in Parentheses)**

atom 1	atom 2	count	d (Å)		
B <sup>e</sup>	B <sup>p,Si</sup>	1×	1.742(2)	skeleton, e–p	
	B <sup>p,Si</sup>	2×	1.760(1)	skeleton o, e–p	
	B <sup>eq</sup>	2×	1.844(1)	skeleton, e–e	
	B <sup>p,B</sup>	1×	1.865(4)	skeleton, e–p	
	B <sup>p,B</sup>	2×	1.905(3)	skeleton, e–p	
	Si <sup>p</sup>	2×	1.990(1)	skeleton, e–p	
	Si <sup>p</sup>	1×	1.989(1)	skeleton, e–p	
	Si <sup>d</sup>	1×	2.0206(7)	exo, with dumbbell	
	Si <sup>p</sup>	1×	1.561(1)	exo, nonexistent	
	B <sup>p,B</sup>	1×	1.664(3)	exo, nonexistent	
Si <sup>p</sup>	B <sup>p,Si</sup>	1×	1.958(2)	exo	
	B <sup>e</sup>	2×	1.990(1)	skeleton, e–p	
	B <sup>e</sup>	1×	1.989(1)	skeleton, e–p	
	B <sup>p,Si</sup>	2×	1.997(2)	skeleton, p–p	
	B <sup>p,B</sup>	2×	2.152(3)	skeleton, p–p	
	Si <sup>p</sup>	2×	2.161(1)	skeleton, p–p	
	B <sup>p,B</sup>	Si <sup>p</sup>	1×	1.664(3)	skeleton, nonexistent
	B <sup>p,B</sup>	1×	1.771(4)	skeleton	
	B <sup>e</sup>	1×	1.865(4)	skeleton, e–p	
	B <sup>e</sup>	2×	1.905(3)	skeleton, e–p	
B <sup>p,Si</sup>	B <sup>p,Si</sup>	2×	1.965(3)	skeleton, p–p	
	B <sup>p,Si</sup>	1×	2.064(4)	skeleton, nonexistent	
	B <sup>p,B</sup>	2×	2.134(4)	skeleton, p–p, nonexistent	
	Si <sup>p</sup>	2×	2.152(3)	skeleton, p–p	
	B <sup>e</sup>	1×	1.742(2)	skeleton, e–p	
	B <sup>e</sup>	2×	1.760(1)	skeleton, e–p	
	B <sup>p,Si</sup>	2×	1.769(2)	skeleton, p–p	
	Si <sup>p</sup>	1×	1.958(2)	exo	
	B <sup>p,B</sup>	2×	1.965(3)	skeleton, p–p	
	Si <sup>p</sup>	2×	1.997(2)	skeleton, p–p	
B <sup>p,Si</sup>	B <sup>p,B</sup>	1×	2.064(4)	exo, nonexistent	
	B <sup>p,Si</sup>	1×	2.357(2)	exo, nonexistent	
	Si <sup>d</sup>	B <sup>e</sup>	3×	2.0206(7)	
	Si <sup>d</sup>	1×	2.4138(5)		
	center	B <sup>e</sup>	6×	1.7502(7)	
	B <sup>p,Si</sup>	6×	1.623(2)		
	B <sup>p,B</sup>	6×	1.914(3)		
	Si <sup>p</sup>	6×	2.0273(9)		

signal of unreacted Si is similar to that reported for bulk Si nanopowder.<sup>78</sup>

The integrated <sup>29</sup>Si MAS NMR signal intensities for the resonances at -64 and 11 ppm yield a icosahedral/dumbbell occupancy ratio of 0.78(4). This implies a composition  $\text{Si}_2(\text{Si}_{1.56}\text{B}_{10.44}) = \text{SiB}_{2.93(7)}$  [25.4(4) atom % of Si] for the bulk  $\alpha\text{-SiB}_{3-x}$  sample. We emphasize that the compositional analysis for single crystals from the refinement diffraction data and for bulk samples from <sup>29</sup>Si MAS NMR experiments are most accurate. Therefore, the conjecture is made that poly/micro-crystalline bulk samples and single-crystal samples (obtained at higher temperatures) of  $\alpha\text{-SiB}_{3-x}$  actually have a different composition. The composition of single crystals is closer to the ideal, electron-precise, composition  $\text{SiB}_{2.5}$ .

In summary, the crystal structure model 4 extracted from high-resolution SC-XRD provides an average structure for disordered  $\alpha\text{-SiB}_{3-x}$  with reasonable geometric parameters and suggests a composition  $\text{SiB}_{2.64(2)}$  for single-crystal samples. The composition of polycrystalline (bulk) samples was established from <sup>29</sup>Si MAS NMR investigations and is more B-rich,  $\text{SiB}_{2.93(7)}$ .

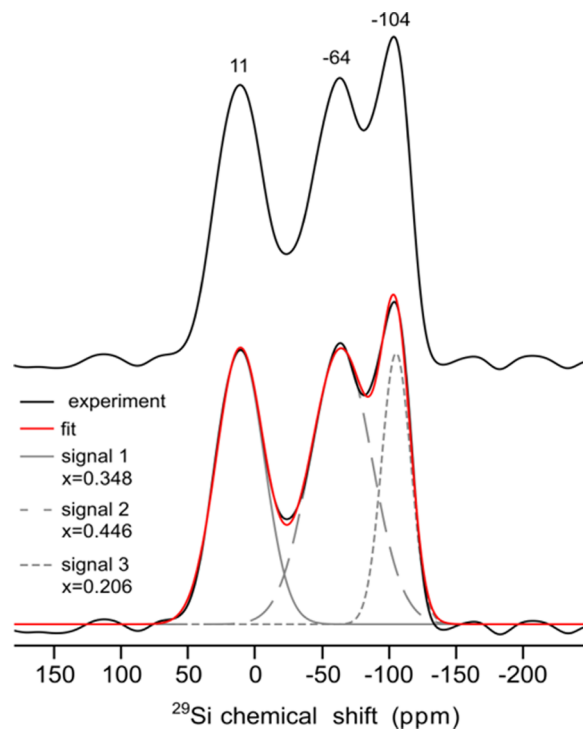


**Figure 10.** <sup>29</sup>Si MAS NMR spectrum of a sample containing both unreacted Si (~20 wt %) and  $\alpha\text{-SiB}_{3-x}$ . The error of the deconvoluted signal contributions is conservatively estimated as 0.35(1), 0.44(1), and 0.21(1). The sample (~300 mg) was prepared from a reaction mixture nano-Si/B = 1:3 (four pellets with 6 mm diameter), heated at 1240 °C for 24 h.

Next we analyze in more detail the structural/occupational disorder in  $\alpha\text{-SiB}_{3-x}$  as well as the relative stability of  $\alpha\text{-SiB}_{3-x}$  with respect to  $\beta\text{-SiB}_3$  by theoretical calculations.

**3.3. Calculated Structural Stability and Electronic Structures.** **3.3.1. Ground-State Search of  $\alpha\text{-SiB}_{2.5}$  and  $\alpha\text{-SiB}_3$ .** To search for the ground-state  $\sigma$  of  $\alpha\text{-SiB}_{3-x}$  via the cluster expansion (CE) method, we first established a database of different  $\sigma$  values of  $\alpha\text{-SiB}_{3-x}$  with  $x$  ranging from 0.5 to -0.67 by using the algorithm developed by Hart and Forcade.<sup>79</sup> For the considered configuration space (42 atoms in a primitive supercell, equivalent to three primitive rhombohedral unit cells), a set of 4826  $\sigma$  was obtained, which distributed over five compositions, i.e.,  $\text{SiB}_{2.5}$ ,  $\text{SiB}_{2.82}$ ,  $\text{SiB}_3$ ,  $\text{SiB}_{3.2}$ , and  $\text{SiB}_{3.67}$ . We singled out the first few hundreds of the generated  $\sigma$ , calculated their total energy using DFT (by the VASP code), and included them in the CE to determine the initial ECIs, using the MAPS code.<sup>62</sup> The obtained initial ECIs were then used to predict the total energy of all generated  $\sigma$  via eq 1. This procedure should reveal the ground-state  $\sigma$ . However, one should be aware that the ECIs determined from the first expansion may not predict the total energy accurately and thus their predictive power needs to be improved. To this end, the total energies predicted by the initial ECIs were utilized as a guideline to single out a few more hundreds of  $\sigma$ , not included in the first expansion. After calculating their total energy by DFT, these  $\sigma$  were included in a second expansion from which ECIs were redetermined. This procedure can be repeatedly performed, until ECIs of desired quality are reached.

The final expansion included 1019  $\sigma$  and employed a total of 70 ECIs. That is, apart from the 0-site and 1-site interactions, the ECIs are composed of 39 two-site interactions and 29 three-site

interactions. The final ECIs fit the 1019 input  $\sigma$  with a cross-validation error of 4.817 meV/site (see Figure S21, Supporting Information), from which the ground-state  $\sigma$  values for the compositions  $\text{SiB}_{2.5}$ ,  $\text{SiB}_3$ , and  $\text{SiB}_{3.67}$  were predicted (see Figure S22, Supporting Information). We note further that DFT-derived and CE-predicted ground-state  $\sigma$  agreed with each other and that no other ground-state  $\sigma$  within 42 atoms/primitive supercell was predicted, thus confirming the predictive power of the final ECIs.

The obtained ground-state  $\sigma$  of  $\alpha\text{-SiB}_{2.5}$  is a 14-atom unit cell and naturally built of  $\text{B}_{10}\text{Si}^{\text{P}}_2$  icosahedra and Si dumbbells. Interestingly, the two  $\text{Si}^{\text{P}}$  atoms are arranged on the same polar triangle, thus forming skeleton (intraicosahedral)  $\text{Si}^{\text{P}}\text{-Si}^{\text{P}}$  bonds as depicted in Figure 11a. This has also been found by An et al. in

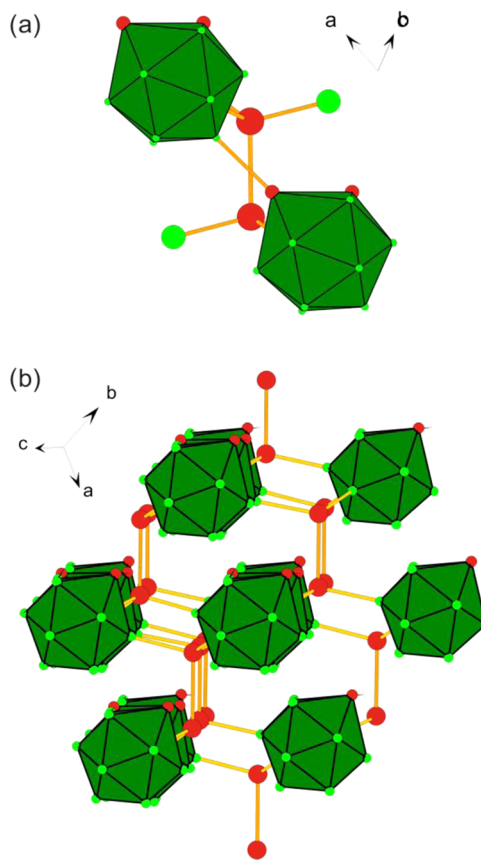


**Figure 11.** Ground-state configurations for  $\alpha\text{-SiB}_{2.5}$  (a) and  $\alpha\text{-SiB}_3$  (b). B and Si atoms are depicted as green and red circles, respectively. The symmetry of  $\alpha\text{-SiB}_{2.5}$  is monoclinic  $Cm$  (depicted is the primitive cell), and the one of  $\alpha\text{-SiB}_3$  is triclinic.

their study of the shear deformation of  $\text{Si}_2(\text{B}_{10}\text{Si}^{\text{P}}_2)$ <sup>31</sup> and is the same arrangement as in molecular 1,2-dimethyl-*ortho*-disilaborane.<sup>28</sup> The interatomic distances, which are compared in Table 7, agree very well. Expectedly, the substitution of  $\text{B}^{\text{P}}$  atoms for  $\text{Si}^{\text{P}}$  results in a significant distortion of  $\text{B}_{10}\text{Si}^{\text{P}}_2$  clusters, and the lattice parameters of the most stable  $\alpha\text{-SiB}_{2.5}$  are found to deviate from the ideal rhombohedral metric. The space group symmetry of the  $\alpha\text{-SiB}_{2.5}$  ground-state  $\sigma$  is monoclinic  $Cm$ . For  $\alpha\text{-SiB}_3$ , the most stable  $\sigma$  at  $T = 0$  K (shown in Figure 11b) is based on a 28-atom primitive supercell. The structure is composed of  $\text{B}_{11}\text{Si}^{\text{P}}$  and  $\text{B}_{10}\text{Si}^{\text{P}}_2$  icosahedra, which are arranged as alternating close-packed layers parallel to the  $ab$  plane in the triclinic unit cell. The

structural parameters of the ground-state  $\sigma$  of  $\alpha\text{-SiB}_{2.5}$  and  $\alpha\text{-SiB}_3$  are reported as Tables 3–6, Supporting Information.

The predicted ground-state  $\sigma$  values of  $\alpha\text{-SiB}_{2.5}$  and  $\alpha\text{-SiB}_3$  compare favorably with the experimental structure (cf. Figure 9 and Table 7). Particularly, the theoretical primitive unit cell volume of  $\alpha\text{-SiB}_{2.5}$  ( $148.7 \text{ \AA}^3$ ) agrees well with the experiment ( $\text{SiB}_{\sim 2.65}$ ,  $147.1 \text{ \AA}^3$ ). Also, the distribution of the distances for the various skeleton bonds:  $\text{B}^{\text{e}}\text{-B}^{\text{e}}$ ,  $\text{B}^{\text{e}}\text{-B}^{\text{P}}$ ,  $\text{B}^{\text{e}}\text{-Si}^{\text{P}}$ ,  $\text{B}^{\text{P}}\text{-B}^{\text{P}}$ ,  $\text{B}^{\text{P}}\text{-Si}^{\text{P}}$ ,  $\text{Si}^{\text{P}}\text{-Si}^{\text{P}}$ , and exo-bonds:  $\text{B}^{\text{P}}\text{-B}^{\text{P}}$ ,  $\text{B}^{\text{P}}\text{-Si}^{\text{P}}$ ,  $\text{B}^{\text{e}}\text{-Si}$ , as well as the Si–Si dumbbell bond match well model 4 obtained from the refinement of high-resolution SC-XRD data (cf. Table 7). When comparing the ground-state  $\sigma$  values of  $\alpha\text{-SiB}_{2.5}$  and  $\alpha\text{-SiB}_3$ , one recognizes a contraction of the primitive unit cell volume from  $148.7$  to  $143.5 \text{ \AA}^3$  (cf. Tables S3 and S4, Supporting Information). This contraction is expected because of the smaller  $\text{B}_{11}\text{Si}^{\text{P}}$  icosahedra compared to  $\text{B}_{10}\text{Si}^{\text{P}}_2$  ones. It is difficult to claim a significant difference between the hexagonal unit cell volume of polycrystalline bulk samples with a composition  $\text{SiB}_{\sim 2.9}$  ( $V_{\text{average}} = 443.7 \text{ \AA}^3$ , cf. Table 3) and of the single crystal sample with a composition  $\text{SiB}_{\sim 2.65}$  ( $V = 441.4 \text{ \AA}^3$ ). The cell volume of the powder samples may also be influenced by configurational disorder and/or the presence of microstrain. The structural parameters of  $\beta\text{-SiB}_3$  are excellently reproduced by our theoretical calculations, as reported in Table S5, Supporting Information. There is virtually no difference in the calculated molar volume of  $\beta\text{-SiB}_3$  ( $V = 41.03 \text{ \AA}^3$ ) and the predicted ground-state  $\sigma$  of  $\alpha\text{-SiB}_3$  ( $41.02 \text{ \AA}^3$ ), cf. discussion of experimental volumes in Section 3.1.

**3.3.2. Phase Stability of  $\alpha\text{-SiB}_{2.5}$  and  $\alpha\text{-SiB}_3$ .** To assess the relative thermodynamic stability of  $\beta\text{-SiB}_3$  and  $\alpha\text{-SiB}_{3-x}$  we computed their energies of formation with respect to  $\alpha\text{-B}_{12}$  and Si. The results, shown in Figure 12, reveal that, despite being stable with respect to the elemental phases, the predicted ground state of  $\alpha\text{-SiB}_{2.5}$  is thermodynamically unstable with respect to the reaction  $6(\alpha\text{-SiB}_{2.5}) = 5(\beta\text{-SiB}_3) + \text{Si}$ , with an enthalpy difference of  $H_0 = 19.17 \text{ meV/atom}$ . We additionally find that the arrangement of  $\text{Si}^{\text{P}}$  atoms on the same polar triangle of the most stable  $\sigma$  of  $\alpha\text{-SiB}_{2.5}$  is favored (by  $\sim 7 \text{ meV/atom}$ ) over distributing the two  $\text{Si}^{\text{P}}$  atoms on the opposite triangles. The formation of intericosahedral  $\text{Si}^{\text{P}}\text{-Si}^{\text{P}}$  exo-bonds, on the other hand, is highly unfavorable (by more than  $1.294 \text{ eV/bond}$ ). The stability of intraicosahedral skeleton  $\text{Si}^{\text{P}}\text{-Si}^{\text{P}}$  bonds is in stark contrast to the situation in the recently proposed high-pressure phase of boron carbide  $\text{B}_{2.5}\text{C}$ . In  $\text{B}_{2.5}\text{C}$ , the energy cost to form skeleton  $\text{C}^{\text{P}}\text{-C}^{\text{P}}$  bonds is about  $0.4 \text{ eV/bond}$ .<sup>29</sup> The lowest-energy  $\sigma$  of  $\alpha\text{-SiB}_3$  is considerably less stable than  $\beta\text{-SiB}_3$ , by  $\sim 30 \text{ meV/atom}$  at  $T = 0$  K, and it is also unstable with respect to  $\alpha\text{-SiB}_{2.5}$  and  $\alpha\text{-B}_{12}$ . The lowest-energy  $\sigma$  of the most boron-rich composition considered,  $\alpha\text{-SiB}_{3.67}$ , is thermodynamically unstable with respect to the elemental phases at  $T = 0$  K.

Although the substitution of  $\text{B}^{\text{P}}$  for  $\text{Si}^{\text{P}}$  results in a distortion which reduces the space group symmetry of the ground-state  $\sigma$  of  $\alpha\text{-SiB}_{2.5}$  to monoclinic ( $Cm$ ), the higher rhombohedral symmetry ( $R\bar{3}m$ ) of  $\alpha\text{-SiB}_{3-x}$  may possibly be restored through the thermally induced configurational disorder of  $\text{Si}^{\text{P}}$  atoms on the polar site of  $\text{B}_{10}\text{Si}^{\text{P}}_2$  icosahedra. The configurational disorder of the  $\text{Si}^{\text{P}}$  atoms, presumably thermodynamically favored at elevated temperature, gives rise to configurational entropy  $S_{\text{conf}}$  which will contribute to the thermodynamic stability of  $\alpha\text{-SiB}_{2.5}$ . Within the mean-field approximation,  $S_{\text{conf}}$  is volume- and temperature-independent and may be derived according to

$$S_{\text{conf}} = k_{\text{B}} \ln(g)$$

**Table 7. Comparison of Interatomic Distances (Å)**

distance	$\alpha\text{-SiB}_{2.5}$	$\alpha\text{-SiB}_3$	experiment (SC-XRD, this work)	$((\text{CH}_3)_2\text{Si}_2\text{B}_{10}\text{H}_{10})$ (ref 28)
skeleton B <sup>e</sup> –B <sup>p</sup>	1.75–1.87	1.76–1.88	1.742, 1.760 × 2	1.77–1.78
s–s			1.865, 1.905 × 2	
skeleton B <sup>e</sup> –B <sup>e</sup>	1.80–1.90	1.74–1.90	1.844 × 2	1.85–1.86
skeleton B <sup>e</sup> –Si <sup>p</sup>	2.02–2.22	2.00–2.11	1.989, 1.990 × 2	2.017, 2.018
skeleton B <sup>p</sup> –B <sup>p</sup>	1.76, 1.85	1.77–1.92	1.771 × 2 1.965 × 2	
skeleton B <sup>p</sup> –Si <sup>p</sup>	2.22	2.11–2.22	1.997 × 2 2.152 × 2	2.113, 2.116
skeleton Si <sup>p</sup> –Si <sup>p</sup>	2.33	2.36	2.161 × 2	2.308
exo B <sup>p</sup> –B <sup>p</sup>	1.75	1.74–1.76	1.771	
exo B <sup>p</sup> –Si <sup>p</sup>	1.98	2.03–2.05	1.958	
exo Si–B <sup>e</sup>	2.03–2.06	1.99–2.06	2.021 × 3	
Si <sup>d</sup> –Si <sup>d</sup>	2.44	2.36, 2.43	2.414	
center–B <sup>e</sup> ,B <sup>p</sup> ,Si <sup>p</sup>	1.68–2.06	1.60–2.06	1.62–2.03	1.71–2.05
		1.70–2.04		

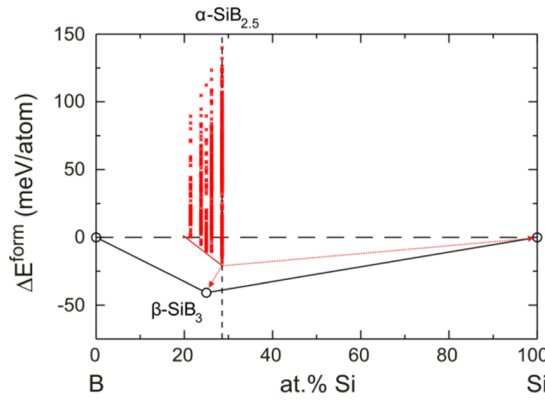


**Figure 12.** Ground-state diagram at 0 K for  $\alpha\text{-SiB}_{3-x}$ , where  $x = 0.5, 0.18, 0, -0.2$ , and  $-0.67$  in relation to thermodynamically stable  $\beta\text{-SiB}_3$ . The red crosses are the DFT calculated formation energies of the 1019 configurations (up to a supercell size of 42 atoms), which were included in the cluster expansion.

where  $g$  is the number of distinguishable ways of arranging the atoms on the lattice sites. The thermodynamic stability of disordered  $\alpha\text{-SiB}_{2.5}$  at zero pressure is then determined by the Gibbs free energy as

$$G(T, p = 0) = H_0 - TS_{\text{conf}}$$

where  $H_0$  is the enthalpy of disordered  $\alpha\text{-SiB}_{2.5}$  at  $T = 0$  K relative to  $\beta\text{-SiB}_3$  and elemental Si. There are six distinguishable configurations to arrange two Si<sup>p</sup> atoms on the same polar triangle of a  $B_{10}\text{Si}^{p2}$  icosahedron, irrespective of the formation of exo-Si<sup>p</sup>–Si<sup>p</sup> bonds. Thus,  $S_{\text{conf}}/(14 \text{ atom unit cell})$  of disordered  $\alpha\text{-SiB}_{2.5}$  is estimated to be  $k_B \ln(6)$ . For simplicity, we used the enthalpy  $H_0$  of the ground-state  $\sigma$  of  $\alpha\text{-SiB}_{2.5}$  instead of the proper enthalpy  $H$  of disordered  $\alpha\text{-SiB}_{2.5}$ , which will overestimate the stability of disordered  $\alpha\text{-SiB}_{2.5}$ . Including  $TS_{\text{conf}}$  and setting  $G(T) = 0$ , disordered  $\alpha\text{-SiB}_{2.5}$  becomes thermodynamically stable with respect to Si and  $\beta\text{-SiB}_3$  at  $T > 1800$  K. Apart from the overestimation of the stability of  $\alpha\text{-SiB}_{2.5}$ , we find that this temperature further increases, if the contributions from the lattice vibrations  $S_{\text{vib}}$  are taken into consideration (see Figure S23, Supporting Information).

Turning to the composition  $\alpha\text{-SiB}_3$ , for which  $\sigma$  is composed of 50%  $B_{10}\text{Si}^{p2}$  and 50%  $B_{11}\text{Si}^p$  icosahedra,  $S_{\text{conf}}$  should be substantially higher compared to that of  $\alpha\text{-SiB}_{2.5}$ , for which  $\sigma$  is

exclusively composed of  $B_{10}\text{Si}^{p2}$  icosahedra. For disordered  $\alpha\text{-SiB}_3$ ,  $S_{\text{conf}}/(28 \text{ atom unit cell})$  is estimated as  $k_B \ln(2 \times 6^2)$  because in addition to the configurational disorder of the Si<sup>p</sup>–Si<sup>p</sup> pairs for  $B_{10}\text{Si}^p$  icosahedra, the Si<sup>p</sup> atoms of  $B_{10}\text{Si}^p$  icosahedra statistically occupy one out of the six polar positions. With this coarse analysis,  $\alpha\text{-SiB}_3$  is predicted to be stable over  $\beta\text{-SiB}_3$  at  $T > 2300$  K. Considering these theoretical results, together with our experimental observations, it turns out clearly that  $\alpha\text{-SiB}_{3-x}$  is merely metastable.

**3.3.3. Electronic Structure.** Figure 13 compares the electronic DOS of the predicted ground-state  $\sigma$  of  $\alpha\text{-SiB}_{2.5}$  and

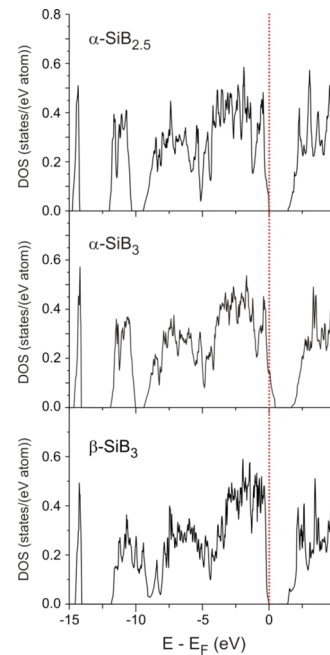


**Figure 13.** Electronic density of states (DOS) for the ground-state configurations of  $\alpha\text{-SiB}_{2.5}$  and  $\alpha\text{-SiB}_3$  (cf. Figure 11), and  $\beta\text{-SiB}_3$ . The red, broken, horizontal line indicates the Fermi level.

$\alpha\text{-SiB}_3$ , as well as the DOS of  $\beta\text{-SiB}_3$ . Expectedly, our simulations reveal that  $\alpha\text{-SiB}_{2.5}$  is a semiconductor with a completely filled valence band due to the electron-precise nature of  $\text{Si}_2(\text{B}_{10}\text{Si}^{p2})$ . On the other hand,  $\alpha\text{-SiB}_3$  is a metal. Such a metallic behavior of  $\alpha\text{-SiB}_3$  can be interpreted by the electron deficiency of the  $B_{11}\text{Si}^p$

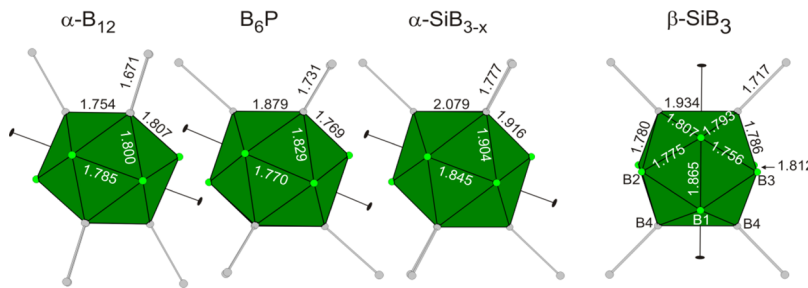


**Figure 14.** Comparison of interatomic distances within icosahedral units and exo-bonds along the series  $\alpha\text{-B}_{12}$ ,  $\text{B}_6\text{P}$ ,  $\alpha\text{-SiB}_{3-x}$  (with mass-weighted average coordinates for the polar position), and  $\beta\text{-SiB}_3$ .

icosahedron, requiring an extra electron to completely fill all of its bonding states. As a result, the existence of  $\text{B}_{11}\text{Si}^{\text{P}}$  icosahedra not only gives rise to unoccupied electronic states (holes) in the valence band but also implies that nonstoichiometric  $\alpha\text{-SiB}_{3-x}$  which is constituted of  $\text{B}_{10}\text{Si}^{\text{P}}_2$  and  $\text{B}_{11}\text{Si}^{\text{P}}$  icosahedra, displays metallic properties. It should, however, be noted that the electron-deficient state of icosahedral boron-rich solids, caused by deviations from their electron-precise compositions, can be compensated by configurational disorder arising either from substitutional and interstitial defects or from vacancies, as recently demonstrated for boron carbides  $\text{B}_{4-x}\text{C}^{21,80-83}$  and boron subnitride  $\text{B}_{6.33}\text{N}^{6,84}$ . It will be important to investigate and characterize the electron transport properties of  $\alpha\text{-SiB}_{3-x}$  in the future, using single-crystal and consolidated polycrystalline specimens [e.g., from spark plasma sintering, cf. Supporting Information (Figure S12)]. Because of their more B-rich composition, the latter are expected to possess a higher carrier concentration.

In contrast to  $\alpha\text{-SiB}_3$ ,  $\beta\text{-SiB}_3$  is a semiconductor. All of the boron atoms in the icosahedra attain an exo-bond and thus the boron substructure can be expressed as  $(\text{B}_{12})^{2-}$ . The negative charge is balanced by the cationic nature of the  $\text{Si}_4$  rhomboid rings, which are electron-precise for an electron count of 3.5e per atom. Thus,  $\beta\text{-SiB}_3$  can be expressed with an ionic formula,  $\text{Si}_4^{2+}(\text{B}_{12})^{2-}$ .<sup>41-43</sup> A detailed bonding analysis based on an experimental charge density study will be the subject of a forthcoming paper.<sup>85</sup>

**3.4. Vibrational Properties.** Vibrational studies of  $\alpha\text{-B}_{12}$ - and  $\alpha\text{-B}_{12}$ -derived refractories have been previously undertaken for investigating fundamental bonding properties of complex structured, “electron-deficient”, solids as well as for analyzing structural disorder and imperfections in these materials.<sup>86-91</sup> Here, we sketch the vibrational property changes, which accompany structure and bonding changes along the sequence  $\alpha\text{-B}_{12}-\text{B}_6\text{P}-\alpha\text{-SiB}_{3-x}-\beta\text{-SiB}_3$ , using Raman spectroscopy.

At this point, it is instructive to have a closer look at the evolution of the icosahedral units across this sequence (shown in Figure 14). For the rhombohedral structures, their local symmetry is  $D_{3d}$ . To compare disordered  $\alpha\text{-SiB}_{3-x}$  mass-weighted average coordinates were employed for the polar position. As introduced earlier, going from  $\alpha\text{-B}_{12}$  to  $\text{B}_6\text{P}$  replaces intericosahedral 3c2c bonding by exo-bonding to  $\text{P}_2$  dumbbells. Naturally, this expands the exo-bond length between polar atoms considerably, as well as widens the distances between polar atoms within the icosahedron (i.e., enlarges the polar triangles of the icoahedron). Going from  $\text{B}_6\text{P}$  to  $\alpha\text{-SiB}_{3-x}$  then leads to highly strained icosahedra. The significantly larger skeleton Si–B distances also cause the (skeleton)  $\text{B}^{\text{e}}-\text{B}^{\text{e}}$  distances being considerably widened compared to  $\text{B}_{12}$  (from 1.78 to 1.85 Å). In orthorhombic  $\beta\text{-SiB}_3$ , icosahedral units attain

a local  $D_{2h}$  symmetry and consisting exclusively of B atoms, which distribute over four crystallographic sites. The distinction between polar and equatorial sites (which is based on rhombohedral symmetry) is not respected. One can note that the skeleton B–B distances are considerably larger compared to  $\alpha\text{-B}_{12}$  and  $\text{B}_6\text{P}$ . This holds especially true for the B4–B4 distances (which exceed 1.9 Å). At the same time, the length of B4–B4 exo-bonds, connecting neighboring icosahedra, corresponds very well to the exo-bond length in  $\text{B}_6\text{P}$  (1.72 vs 1.73 Å).

The Raman spectra of  $\alpha\text{-B}_{12}$ ,  $\text{B}_6\text{P}$ ,  $\alpha\text{-SiB}_{3-x}$ , and  $\beta\text{-SiB}_3$  are compiled in Figure 15. According to group theory, there are 10 Raman-active modes for  $\alpha\text{-B}_{12}$ , which distribute according to four  $A_{1g}$  and six  $E_g$ . The modes were first assigned by Beckel et al.,<sup>92</sup> a more recent discussion is given in ref 86. The pair of  $A_{1g}$  and  $E_g$  bands at highest wavenumbers (at 1187 and 1122  $\text{cm}^{-1}$ , respectively) is associated with stretching modes of exo-bonded  $\text{B}^{\text{P}}$  atoms connecting icosahedra. The next  $A_{1g}$  and  $E_g$  pair (at 931 and 871  $\text{cm}^{-1}$ , respectively) is associated with localized icosahedral (skeleton) modes. The  $A_{1g}$  mode at 793  $\text{cm}^{-1}$  corresponds to a radially in-and-out (breathing) movement of  $\text{B}^{\text{e}}$  atoms and thus can be associated with a stretching mode of the 3c bonds. In the  $E_g$  mode at 774  $\text{cm}^{-1}$ , 2c and 3c bonds are strained significantly. The  $E_g$  mode at 710  $\text{cm}^{-1}$  is associated with a deformation of polar triangles and thus relates to deformation/bending of exo-bonds between  $\text{B}^{\text{P}}$  atoms. The pair of  $A_g$  and  $E_g$  bands at 691 and 598  $\text{cm}^{-1}$ , respectively, may be associated with bending of 3c bonds. Finally, the sharp line at 523  $\text{cm}^{-1}$  (which is a  $E_g$  mode) corresponds to libration of icosahedra.

The Raman spectrum of  $\text{B}_6\text{P}$  can be easily related to  $\alpha\text{-B}_{12}$ . The phonon states of  $\text{B}_6\text{P}$  have been recently calculated, and its Raman spectrum was analyzed.<sup>93</sup> There are five  $A_{1g}$  and seven  $E_g$  modes. The  $A_{1g} + E_g$  pair associated with changes of the 3c bonds (equatorial breathing and bending) in  $\alpha\text{-B}_{12}$  will blue-shift upon exchange of the 3c-bond for exo-bonds to P atoms. At the same time, the modes associated with stretching of  $\text{B}^{\text{P}}-\text{B}^{\text{P}}$  exo-bonds will red-shift because of their substantially increased length compared to  $\alpha\text{-B}_{12}$  (cf. Figure 14). As a consequence, all modes associated with stretching of exo-bonds (i.e., both  $\text{B}^{\text{P}}-\text{B}^{\text{P}}$  and  $\text{B}^{\text{e}}-\text{P}$ ) fall in a narrow range 1000–1100  $\text{cm}^{-1}$ . The removal of 3c-bonds (through the introduction of the  $\text{P}_2$  units) leads also to more individual (localized) skeleton modes, which fall in the range 630–830  $\text{cm}^{-1}$ . Skeleton modes are red-shifted with respect to  $\alpha\text{-B}_{12}$  because of the “enlarged” icosahedra in  $\text{B}_6\text{P}$ . The location of the  $\text{B}_{12}$  libration mode is essentially maintained. Lower-frequency modes are then associated with the  $\text{P}_2$  dumbbells. The  $A_g$  mode at 479  $\text{cm}^{-1}$  corresponds to the P–P stretching mode. The  $E_g$  mode at 373  $\text{cm}^{-1}$  corresponds to a P–B bending mode arising from a rotational movement/displacement of the  $\text{P}_2$  entity.

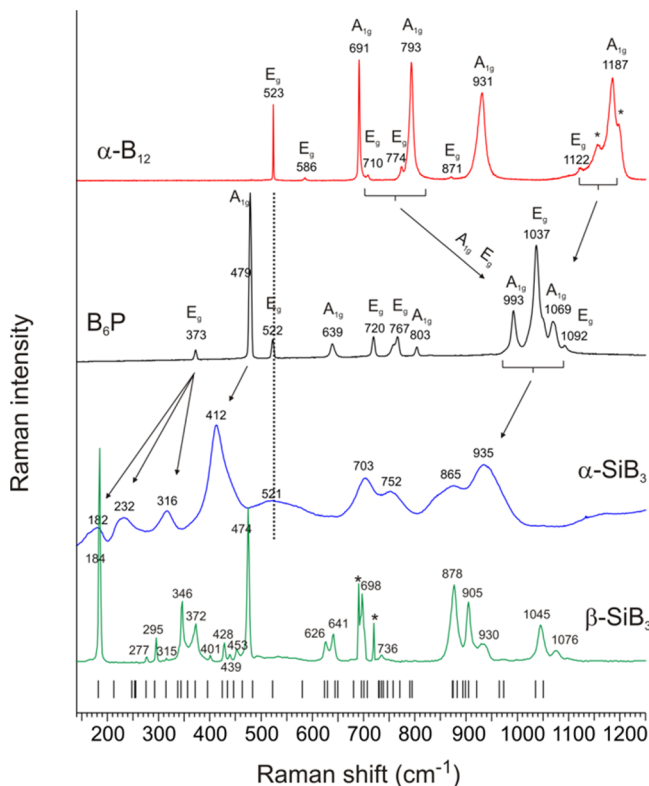


**Figure 15.** Raman spectra of  $\alpha\text{-B}_{12}$ ,  $\text{B}_6\text{P}$ ,  $\alpha\text{-SiB}_{3-x}$ , and  $\beta\text{-SiB}_3$  single crystals (from top to bottom). The  $\alpha\text{-B}_{12}$ ,  $\alpha\text{-SiB}_{3-x}$  and  $\beta\text{-SiB}_3$  spectra were recorded from samples prepared for this work, whereas the spectrum of  $\text{B}_6\text{P}$  was provided by Reshetniak and corresponds to that described in ref 93. For  $\alpha\text{-B}_{12}$  and  $\text{B}_6\text{P}$ , the symmetry of the modes is indicated. The arrows indicate the relation of modes in the spectra of  $\alpha\text{-B}_{12}$  and  $\text{B}_6\text{P}$ , and  $\text{B}_6\text{P}$  and  $\alpha\text{-SiB}_{3-x}$ . The horizontal dotted line marks the location of the libration mode in the spectra of  $\alpha\text{-B}_{12}$ ,  $\text{B}_6\text{P}$ , and  $\alpha\text{-SiB}_{3-x}$ . The bars underneath the spectrum of  $\beta\text{-SiB}_3$  correspond to DFT calculated Raman modes for  $\beta\text{-SiB}_3$ . The asterisks in the  $\beta\text{-SiB}_3$  spectrum mark possibly spurious peaks. The asterisks in the  $\alpha\text{-B}_{12}$  spectrum mark bands due to luminescence and/or  $^{10}\text{B}/^{11}\text{B}$  isotope effects.<sup>86</sup>

When going from  $\text{B}_6\text{P}$  to  $\alpha\text{-SiB}_{3-x}$  it is obvious that the sharp modes for ordered  $\alpha\text{-B}_{12}$  and  $\text{B}_6\text{P}$  become broad bands. This has already been described by Aselage and Tallant.<sup>94</sup> Bands associated with exo-bonds (both B–B and B–Si) fall in a range 850–1000 cm<sup>-1</sup>, whereas skeleton modes are essentially confined between 650 and 800 cm<sup>-1</sup> (but distribute partially to even lower wavenumbers). The hump at 521 cm<sup>-1</sup> may be associated with libration. The Si–Si stretching mode of the dumbbell may be suspected at 412 cm<sup>-1</sup>. However, the analysis of calculated phonons (see below) shows that also the displacement of Si atoms on the polar position falls in this range of wavenumber. This is in agreement with the vibrational spectrum of 1,2-dimethyl-*ortho*-disilaborane, ( $\text{CH}_3\text{}_2\text{Si}_2\text{B}_{10}\text{H}_{10}$ ).<sup>28</sup> Additional modes at lower wavenumbers are associated with  $\text{Si}_2$  dumbbell rotations and translations, coupled with displacements of Si atoms, which are part of the icosahedron. This information was obtained from an inspection of the phonon DOS (pDOS) of  $\alpha\text{-SiB}_{2.5}$  structural models (see below) and the analysis of frequencies and displacements at the  $\Gamma$  point.

Turning lastly to the spectrum of  $\beta\text{-SiB}_3$ , one notes first the sharp Raman lines because of its well-ordered crystalline structure. Of the 93 optical modes of  $\beta\text{-SiB}_3$ , 48 are Raman-

active. About 30 are clearly visible in the spectrum shown in Figure 15. Their DFT calculated wavenumbers are included in this figure. Above 1000 cm<sup>-1</sup> modes are associated with B–B exo-bonds, which are between B4 atoms (cf. Figure 14). The B–B exo-bond length in  $\beta\text{-SiB}_3$  is reduced with respect to  $\alpha\text{-SiB}_3$ , but similar to that of  $\text{B}_6\text{P}$ . At lower wavenumbers, one first notes two groups of bands, which are located between 600 and 750 cm<sup>-1</sup> and 870 and 950 cm<sup>-1</sup>. The former correspond predominately to icosahedron (skeleton) modes, whereas the latter relate to Si–B exo-bonds. Modes below 500 cm<sup>-1</sup> are then associated with Si–Si vibrations within the zigzag chain structure of  $\text{Si}_4$  rhomboid rings (cf. Figure 2). The mode at 474 cm<sup>-1</sup> corresponds to the stretch between two Si1 atoms, which connect rhomboid ring units. This Si–Si bond length (2.33 Å) is similar to that of elemental Si (2.35 Å) and, thus, considerably shorter than the distance between Si atoms forming dumbbells in  $\alpha\text{-SiB}_{3-x}$ . The intense band at 184 cm<sup>-1</sup> is associated with the breathing mode of a  $\text{Si}_4$  rhomboid unit.

Figure 16 depicts the phonon DOS of the  $\alpha\text{-SiB}_{2.5}$  ground-state configuration and  $\beta\text{-SiB}_3$ . As mentioned above, the

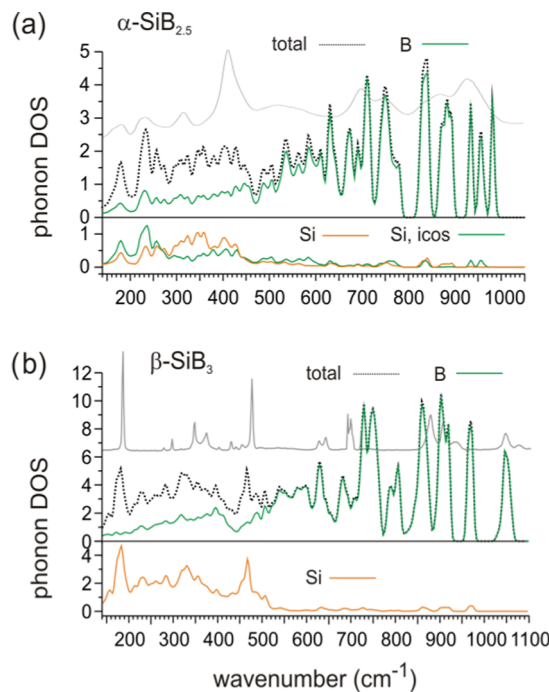


**Figure 16.** Calculated phonon density of states (pDOS) for  $\alpha\text{-SiB}_{2.5}$  (a) and  $\beta\text{-SiB}_3$  (b), cf. Figure 11. The total pDOS is depicted as the broken, black line. The partial pDOS of icosahedron and dumbbell forming atoms are shown as green and orange lines, respectively. For comparison, the Raman spectra are included at the top of each panel (in light gray).

calculated pDOS were used to assist in the assignment of Raman modes and vibrational bands shown in Figure 15. Modes at highest wavenumber involve exclusively boron atoms. The localized nature of the modes associated with Si–Si stretch and  $\text{Si}_4$  breathing in  $\beta\text{-SiB}_3$  manifest as spikes in the pDOS. Their location is well reproduced in the calculations. The pDOS of  $\beta\text{-SiB}_3$  shows states between 500 and 600 cm<sup>-1</sup>, 750 and 850 cm<sup>-1</sup>, and at 950 cm<sup>-1</sup> where there are gaps in the Raman spectrum. Selection rules are not applicable for disordered  $\alpha\text{-SiB}_{3-x}$  and its Raman spectrum resembles an envelope of the pDOS.

#### 4. CONCLUSIONS

We investigated the interplay between the binary silicon boride phases  $\alpha\text{-SiB}_{3-x}$  and  $\beta\text{-SiB}_3$  which have a similar composition but very different crystal structures.  $\alpha\text{-SiB}_{3-x}$  is disordered and nonstoichiometric, with a homogeneity range  $0.1 < x < 0.45$ . Its structure relates to the  $\alpha$ -rhombohedral phase of boron ( $\alpha\text{-B}_{12}$ ) and features  $\text{Si}_2$  dumbbell units at the location of intericosahedral  $3\text{c}2\text{e}$  bonds in  $\alpha\text{-B}_{12}$ . Additionally, Si replaces partly (25–30%) B atoms from the polar position of icosahedral units. Accordingly, the  $\alpha\text{-SiB}_{3-x}$  structure consists of a mixture of  $\text{B}_{10}\text{SiP}_2$  and  $\text{B}_{11}\text{SiP}$  clusters, which are highly strained because of the rather large size difference between B and Si atoms. In the structure model deduced from high-resolution SC-XRD data, the polar position is split into three sites (one Si and two B), which accounts well for the disparity of interatomic distances introduced by the occupational disorder of differently sized atoms. In contrast, the structure of  $\beta\text{-SiB}_3$  is completely ordered with respect to B and Si sites. The Si partial structure constitutes polymeric zigzag chains of rhomboid  $\text{Si}_4$  rings. Boron atoms form  $\text{B}_{12}$  icosahedra, in which all of the B atoms attain an exobond to either a B atom of a neighboring  $\text{B}_{12}$  unit or a silicon atom within the rhomboid chains. The highly ordered nature of  $\beta\text{-SiB}_3$  is reflected in its Raman spectrum, which features narrow and distinct lines. In contrast, the Raman spectrum of  $\alpha\text{-SiB}_{3-x}$  is characterized by broad bands, which nevertheless show a clear relation to the vibrational modes of isostructural, ordered,  $\text{B}_6\text{P}$ .

$\alpha\text{-SiB}_{3-x}$  is metastable with respect to  $\beta\text{-SiB}_3$  and Si, and its formation is kinetically driven. Polycrystalline bulk samples can be obtained within hours when heating binary reaction mixtures at temperatures 1200–1300 °C. Thermodynamically stable  $\beta\text{-SiB}_3$  forms when dwelling binary reaction mixtures at temperatures 1175–1200 °C for extended periods of time (days to weeks). The slow kinetics of  $\beta\text{-SiB}_3$  formation can be overcome by the application of high pressure (5–8 GPa). The fast kinetics of  $\alpha\text{-SiB}_{3-x}$  formation can be exploited for simultaneous synthesis and consolidation of specimens using spark plasma sintering. Both  $\alpha\text{-SiB}_{3-x}$  and  $\beta\text{-SiB}_3$  convert into  $\text{SiB}_6$  and Si at temperatures above 1250 °C.

Poly/microcrystalline bulk samples and single-crystal samples of  $\alpha\text{-SiB}_{3-x}$  have a different composition. The composition of single crystals is closer to the ideal, electron-precise, composition  $\text{SiB}_{2.5}$ . Electronic structure calculations yield band gaps of similar size for  $\alpha\text{-SiB}_{2.5}$  and  $\beta\text{-SiB}_3$ , around 2 eV. Experimentally obtained  $\alpha\text{-SiB}_{3-x}$  ( $0.1 < x < 0.45$ ) should correspond to a p-type conductor. However, the electron transport properties of  $\alpha\text{-SiB}_{3-x}$  are yet unknown, and it will be important to characterize them, along with other physical properties, to assess its potential as a technologically significant material.

#### ■ ASSOCIATED CONTENT

##### S Supporting Information

The Supporting Information is available free of charge on the ACS Publications website at DOI: [10.1021/acsomega.9b02727](https://doi.org/10.1021/acsomega.9b02727).

Compilation of PXRD patterns of products from various reaction mixtures after dwelling in a DSC/TG apparatus in Ar atmosphere (Figures S1–S8); summary of synthesis results using micron-Si and amorphous boron as starting materials (Figure S9); PXRD patterns of  $\beta\text{-SiB}_3$  samples (Figure S10); thermal stability investigation of  $\alpha\text{-SiB}_{3-x}$  and  $\beta\text{-SiB}_3$  (Figure S11); synthesis of  $\alpha\text{-SiB}_{3-x}$  by spark plasma sintering (Figure S12); scanning electron

microscopy (SEM) investigation and EDX analysis of cross section polished Si–B reaction pellets (Figures S13 and S14); SEM investigations and EDX analysis of  $\alpha\text{-SiB}_{3-x}$  single-crystal specimens (Figure S15); SEM/PXRD analysis of starting materials (Figures S16–S19); probability density isosurface for  $\alpha\text{-SiB}_{3-x}$  model 4 (Figure S20); anharmonic ADP values for  $\text{Si}^d$  and  $\text{B}^e$  (Tables S1 and S2); cross-validation plot of cluster expansion (CE) for  $\alpha\text{-SiB}_{3-x}$  (Figure S21); comparison of DFT calculated formation energies with predicted ones using the CE method (Figure S22); vibrational entropy vs  $T$  for  $\alpha\text{-SiB}_{2.5}$  (Figure S23); and structure parameters and interatomic distances of DFT optimized  $\alpha\text{-SiB}_{2.5}$ ,  $\alpha\text{-SiB}_3$ ,  $\beta\text{-SiB}_3$  (Tables S3–S6) ([PDF](#))

#### ■ AUTHOR INFORMATION

##### Corresponding Author

\*E-mail: [Ulrich.Haussermann@mmlk.su.se](mailto:Ulrich.Haussermann@mmlk.su.se).

##### ORCID

Aleksander Jaworski: [0000-0002-7156-559X](#)

Andrew J. Pell: [0000-0002-2542-8113](#)

Michael Widom: [0000-0001-5972-5696](#)

Wolfgang Scherer: [0000-0002-9307-082X](#)

Ulrich Häussermann: [0000-0003-2001-4410](#)

##### Notes

The authors declare no competing financial interest.

#### ■ ACKNOWLEDGMENTS

This work was supported by the Swedish Research Council, the National Science Foundation through grant DMR-1007557, and the Deutsche Forschungsgemeinschaft (SCHE 487/12-1). M.W. was supported by the U.S. Department of Energy grant DE-SC0014506. A.E. gratefully acknowledges the financial support from Ratchadaphiseksomphot Endowment Fund, Chulalongkorn University; Grants for Development of New Faculty Staff. B.A. acknowledges support from the Swedish Foundation for Strategic Research (SSF) through the Future Research Leaders program. S.I.S. and B.A. acknowledges support from the Swedish Government Strategic Research Area in Materials Science on Advanced Functional Materials at Linköping University (Faculty Grant SFO-Mat-LiU No. 2009-00971). A.J. and A.J.P. acknowledge support from the Swedish Research Council (2016-03441). The authors acknowledge the supercomputing resources supported by the Swedish National Infrastructure for Computing (SNIC) performed at the National Supercomputer Centre (NSC) and the High Performance Computing Center North (HPC2N). They are grateful to V.V. Reshetniak for providing them with the Raman spectrum of  $\text{B}_6\text{P}$ .

#### ■ REFERENCES

- (1) Emin, D. Icosahedral Boron-Rich Solids. *Phys. Today* **1987**, *40*, 55–62.
- (2) Lundström, T.; Andreev, Y. G. Superhard boron-rich borides and studies of the B-C-N system. *Mater. Sci. Eng., A* **1996**, *209*, 16–22.
- (3) Slack, G. A.; Morgan, K. E. Some crystallography, chemistry, physics, and thermodynamics of  $\text{B}_{12}\text{O}$ ,  $\text{B}_{12}\text{P}$ ,  $\text{B}_{12}\text{As}$ , and related alpha-boron crystals. *J. Phys. Chem. Solids* **2014**, *75*, 1054–1074.
- (4) Slack, G. A.; McNelly, T. F.; Taft, E. A. Melt growth and properties of  $\text{B}_6\text{P}$  crystals. *J. Phys. Chem. Solids* **1983**, *44*, 1009–1013.

- (5) Hubert, H.; Devouard, B.; Garvie, L. A. J.; O'Keeffe, M.; Buseck, P. R.; Petuskey, W. T.; McMillan, P. F. Icosahedral packing of  $B_{12}$  icosahedra in boron suboxide ( $B_6O$ ). *Nature* **1998**, *391*, 376–378.
- (6) Zhang, H.; Yao, S.; Widom, M. Predicted phase diagram of boron-carbon-nitrogen. *Phys. Rev. B* **2016**, *93*, No. 144107.
- (7) Emin, D. Unusual properties of icosahedral boron-rich solids. *J. Solid State Chem.* **2006**, *179*, 2791–2798.
- (8) Kunka, C.; Yang, X.; An, Q.; Subhash, G. Icosahedral superstrength at the nanoscale. *Phys. Rev. Mater.* **2018**, *2*, No. 063606.
- (9) Werheit, H.; Mori, T.; Ghosh, D.; Subhash, G.; Lassoued, S.; Gautier, R.; Halet, J. F. In *Boron Rich Solids: Sensors, Ultra High Temperature Ceramics, Thermoelectrics, Armor*, Proceedings of the NATO Advanced Research Workshop on Boron Rich Solids: Sensors for Biological and Chemical Detection, Ultra High Temperature Ceramics, Thermoelectrics, Armor, Orlando, Dec 14–18, Orlovskaya, N., Lugovy, M., Eds.; Springer: Dordrecht, 2009; pp 45–114.
- (10) Zhao, Z.; Xu, B.; Tian, Y. Recent Advances in Superhard Materials. *Annu. Rev. Mater. Res.* **2016**, *46*, 383–406.
- (11) Li, D.; Ching, W. Y. Fundamental studies on the structures and properties of some  $B_{12}$ -based crystals. *Phys. Rev. B* **1995**, *52*, 17073–17083.
- (12) Balakrishnarajan, M. M.; Pancharatna, P. D.; Hoffmann, R. Structure and bonding in boron carbide: The invincibility of imperfections. *New J. Chem.* **2007**, *31*, 473–485.
- (13) Albert, B.; Hillebrecht, H. Boron: Elementary Challenge for Experimenters and Theoreticians. *Angew. Chem., Int. Ed.* **2009**, *48*, 8640–8668.
- (14) Will, G.; Kiefer, B. Electron Deformation Density in Rhombohedral  $\alpha$ -boron. *Z. Anorg. Allg. Chem.* **2001**, *627*, 2100–2104.
- (15) Longuet-Higgins, H. C.; Roberts, M.; Roberts, M. d. V. The electronic structure of an icosahedron of boron atoms. *Proc. R. Soc. A* **1955**, *230*, 110–119.
- (16) Wade, K. The Structural Significance of the Number of Skeletal Bonding Electron-pairs in Carboranes, the Higher Boranes and Borane Anions, and Various Transition-metal Carbonyl Cluster Compounds. *J. Chem. Soc., Chem. Commun.* **1971**, 792–793.
- (17) Wade, K. Skeletal Electron Counting in Cluster Species. Some Generalizations and Predictions. *Inorg. Nucl. Chem. Lett.* **1972**, *8*, 559–562.
- (18) Müller, U. *Inorganic Structural Chemistry*, 2nd ed.; John Wiley & Sons Ltd.: Chichester, 2006; pp 116–121.
- (19) Werheit, H. Boron carbide: Consistency of components, lattice parameters, fine structure and chemical composition makes the complex structure reasonable. *Solid State Sci.* **2016**, *60*, 45–54.
- (20) Kurakevych, O. O.; Solozhenko, V. L. Rhombohedral boron subnitride,  $B_{13}N_2$ , by X-ray powder diffraction. *Acta Crystallogr. C* **2007**, *63*, i80–i82.
- (21) Ektarawong, A.; Simak, S. I.; Hultman, L.; Birch, J.; Alling, B. First principles study of configurational disorder in  $B_4C$  using a superatomic-special quasirandom structure method. *Phys. Rev. B* **2014**, *90*, No. 024204.
- (22) Ektarawong, A. Thermodynamic consideration and ground-state search of icosahedral boron subselenide  $B_{12}(B_{1-x}Se_x)_2$  from a first-principles cluster expansion. *Phys. Rev. B* **2018**, *97*, No. 174103.
- (23) Moissan, H.; Stock, A. Ueber die beiden Borsiliciumverbindungen  $SiB_3$  und  $SiB_6$ . *Ber. Dtsch. Chem. Ges.* **1900**, *33*, 2125–2131.
- (24) Magnusson, B.; Brosset, C.; et al. The Crystal Structure of  $B_{2.89}$ . *Acta Chem. Scand.* **1962**, *16*, 449–455.
- (25) Winter, M. Covalent Radii. *WebElements™* [Online]; University of Sheffield: U.K., Posted Dec 4, 2015. [https://www.webelements.com/periodicity/covalent\\_radius/](https://www.webelements.com/periodicity/covalent_radius/) (accessed June 10, 2019).
- (26) Grimes, R. N. *Carboranes*, 3rd ed.; Academic Press: Amsterdam, 2016; pp 283–616.
- (27) Wesemann, L.; Hosmane, N. S. Heteropolyboranes with the Heavier Group 14. In *Molecular Clusters of the Main Group Elements*; Driess, M., Nöth, H., Eds.; Wiley-VCH: Weinheim, 2004; pp 310–321.
- (28) Seyferth, D.; Büchner, K. D.; Rees, W. S., Jr.; Wesemann, L.; Davis, W. M.; Bukalov, S. S.; Leites, L. A.; Bock, H.; Solouki, B. 1,2-Dimethyl-1,2-disila-closo-dodecaborane(12), a Silicon Analog of an  $\sigma$ -Carborane: Synthesis; X-ray Crystal Structure; NMR, Vibrational, and Photoelectron Spectra; Bonding. *J. Am. Chem. Soc.* **1993**, *115*, 3586–3594.
- (29) Ektarawong, A.; Simak, S. I.; Alling, B. Carbon-rich icosahedral boron carbides beyond  $B_4C$  and their thermodynamic stabilities at high temperature and pressure from first principles. *Phys. Rev. B* **2016**, *94*, No. 054104.
- (30) An, Q.; Goddard, W. A., III Microalloying boron carbide with silicon to achieve dramatically improved ductility. *J. Phys. Chem. Lett.* **2014**, *5*, 4169–4174.
- (31) An, Q.; Goddard, W. A., III Improved ductility of  $B_{12}$  icosahedra-based superhard materials through icosahedral slip. *J. Phys. Chem. C* **2017**, *121*, 11831–11838.
- (32) Knarr, W. A. A Study of the Silicon Boron Phases and a Determination of the Enthalpy of Vaporization and Formation of Silicon Hexaboride. Ph.D. Thesis, University of Kansas, Jan 1960.
- (33) Arabe, B. G. Interaction in the system Si-B. *Inorg. Mater.* **1979**, *15*, 1251–1254. A translation of *Izv. An. Nauk SSSR, Neorg. Mater.* **1977**, *15*, 1589–1592.
- (34) Mostafa, A.; Medraj, M. Binary phase diagrams and thermodynamic properties of silicon and essential doping elements (Al, As, B, Bi, Ga, In, N, P, Sb and Ti). *Materials* **2017**, *10*, No. 676.
- (35) Seifert, H. J.; Aldinger, F. Phase Equilibria in the Si–B–C–N System. In *High Performance Non-Oxide Ceramics I*; Mingos, D. M. P., Jansen, M., Eds.; Springer: Berlin, 2002; pp 1–58.
- (36) Fries, S.; Lukas, H. L. System B–Si. In *COST 507. Thermochemical Database for Light Metal Alloys*; Ansara, I., Dinsdale, A. T., Rand, M. H., Eds.; Office for Official Publications of the European Community: Luxembourg, 1998; Vol. 2, pp 126–128.
- (37) Brosset, C.; Magnusson, B. The Silicon-Boron system. *Nature* **1960**, *187*, 54–55.
- (38) Colton, E. On the boron-silicon reaction. *J. Inorg. Nucl. Chem.* **1961**, *17*, 108–111.
- (39) Aselage, T. L. The coexistence of silicon borides with boron-saturated silicon: Metastability of  $SiB_3$ . *J. Mater. Res.* **1998**, *13*, 1786–1794.
- (40) Salvador, J. R.; Bilc, D.; Mahanti, S. D.; Kanatzidis, M. G. Stabilization of  $\beta$ - $SiB_3$  from Liquid Ga: A Boron-Rich Binary Semiconductor Resistant to High-Temperature Air Oxidation. *Angew. Chem., Int. Ed.* **2003**, *42*, 1929–1932.
- (41) Balakrishnarajan, M. M.; Hoffmann, R. Electron-deficient bonding in rhomboid rings. *J. Am. Chem. Soc.* **2004**, *126*, 13119–13131.
- (42) Mikhaylushkin, A. S.; Nylen, J.; Häussermann, U. Structure and Bonding of Zinc Zntimonides: Complex Frameworks and Narrow Band Gaps. *Chem. – Eur. J.* **2005**, *11*, 4912–4920.
- (43) Häussermann, U.; Mikhaylushkin, A. S. Electron-poor antimonides: complex framework structures with narrow band gaps and low thermal conductivity. *Dalton Trans.* **2010**, *39*, 1036–1045.
- (44) Hirsche, B. Synthese, Einkristallzüchtung und Charakterisierung von binären Siliciumboriden. Ph.D. Thesis, Universität Bayreuth, July 2005.
- (45) Kanatzidis, M. G.; Pöttgen, R.; Jeitschko, W. The metal flux: A preparative tool for the exploration of intermetallic compounds. *Angew. Chem., Int. Ed.* **2005**, *44*, 6996–7023.
- (46) Stoyanov, E.; Häussermann, U.; Leinenweber, K. Large-volume multianvil cells designed for chemical synthesis at high pressures. *High Pressure Res.* **2010**, *30*, 175–189.
- (47) Rodríguez-Carvajal, J. In *FULLPROF: A Program for Rietveld Refinement and Pattern Matching Analysis*, Abstracts of the Satellite Meeting on Powder Diffraction of the XV IUCr Congress, 1990; p 127.
- (48) Vlasse, M.; Slack, G. A.; Garbauskas, M.; Kasper, J. S.; Viala, J. C. The crystal structure of  $SiB_6$ . *J. Solid State Chem.* **1986**, *63*, 31–45.
- (49) Dollase, W. A. Correction of intensities for preferred orientation in powder diffractometry: application of the March model. *J. Appl. Crystallogr.* **1986**, *19*, 267–272.
- (50) APEX2, version 2014.3; Bruker-AXS: Madison, Wisconsin, 2014.
- (51) SADABS, v2014/2; Bruker-AXS: Madison, Wisconsin, 2014.

- (52) Petricek, V.; Dusek, M.; Palatinus, L. Crystallographic Computing System JANA2006: General features. *Z. Kristallogr. - Cryst. Mater.* **2014**, *229*, 345–352.
- (53) Hohenberg, P.; Kohn, W. Inhomogeneous electron gas. *Phys. Rev.* **1964**, *136*, B864–B871.
- (54) Kohn, W.; Sham, L. F. Self-consistent equations including exchange and correlation effects. *Phys. Rev.* **1965**, *140*, A1133–A1138.
- (55) Blöchl, P. E. Projector augmented-wave method. *Phys. Rev. B* **1994**, *50*, 17953–17979.
- (56) Kresse, G.; Furthmüller, J. Efficiency of ab-initio total energy calculations for metals and semiconductors using a plane-wave basis set. *Comput. Mater. Sci.* **1996**, *6*, 15–50.
- (57) Kresse, G.; Furthmüller, J. Efficient iterative schemes for ab initio total-energy calculations using a plane-wave basis set. *Phys. Rev. B* **1996**, *54*, 11169–11186.
- (58) Perdew, J.; Burke, K.; Ernzerhof, M. Generalized Gradient Approximation Made Simple. *Phys. Rev. Lett.* **1996**, *77*, 3865–3868.
- (59) Monkhorst, H. J.; Pack, J. D. Special points for Brillouin-zone integrations. *Phys. Rev. B* **1976**, *13*, 5188–5192.
- (60) Blöchl, P. E.; Jepsen, O.; Andersen, O. K. Improved tetrahedron method for Brillouin-zone integrations. *Phys. Rev. B* **1994**, *49*, 16223–16233.
- (61) Sanchez, J. M.; Ducastelle, F.; Gratias, D. Generalized cluster description of multicomponent systems. *Phys. A* **1984**, *128*, 334–350.
- (62) van de Walle, A.; Ceder, G. Automating First-Principles Phase Diagram Calculations. *J. Phase Equilib.* **2002**, *23*, 348–359.
- (63) van de Walle, A.; Asta, M.; Ceder, G. The Alloy Theoretic Automated Toolkit: A User Guide. *CALPHAD* **2002**, *26*, 539–553.
- (64) Togo, A.; Oba, F.; Tanaka, I. First-principles calculations of the ferroelastic transition between rutile-type and CaCl<sub>2</sub>-type SiO<sub>2</sub> at high pressures. *Phys. Rev. B* **2008**, *78*, No. 134106.
- (65) Togo, A.; Tanaka, I. First principles phonon calculations in material science. *Scr. Mater.* **2015**, *108*, 1–5.
- (66) Parlinski, K.; Li, Z. Q.; Kawazoe, Y. First-Principles Determination of the Soft Mode in Cubic ZrO<sub>2</sub>. *Phys. Rev. Lett.* **1997**, *78*, 4063–4066.
- (67) Matkovich, V. I. A new form of boron silicide, B<sub>4</sub>Si. *Acta Crystallogr.* **1960**, *13*, 679–680.
- (68) Rizzo, H. F.; Bidwell, L. R. Formation and structure of SiB<sub>4</sub>. *J. Am. Ceram. Soc.* **1960**, *43*, 550–551.
- (69) Cline, C. F.; Sands, D. E. A new silicon boride, SiB<sub>4</sub>. *Nature* **1960**, *185*, 456.
- (70) Colton, E. Preparation of tetraboron silicide, B<sub>4</sub>Si. *J. Am. Chem. Soc.* **1960**, *82*, 1002.
- (71) Lugscheider, E.; Reimann, H.; Quadakkers, W.-J. Das System Bor-Silicium. *Ber. Dtsch. Keram. Ges.* **1979**, *56*, 301–305.
- (72) Tremblay, R.; Angers, R. Preparation of high purity SiB<sub>4</sub> by solid state reaction between Si and B. *Ceram. Int.* **1989**, *15*, 73–78.
- (73) Vlasse, M.; Viala, J. C. The Boron-Silicon Solid Solution: A Structural Study of the SiB<sub>~36</sub> Composition. *J. Solid State Chem.* **1981**, *37*, 181–188.
- (74) Vick, G. L.; Whittle, K. M. Solid Solubility and Diffusion Coefficients of Boron in Silicon. *J. Electrochem. Soc.* **1969**, *116*, 1142–1144.
- (75) Hung, V. V.; Hong, P. T. T.; Khue, B. V. Boron and phosphorous diffusion in silicon: interstitial, vacancy and combination mechanisms. *Proc. Natl. Conf. Theor. Phys.* **2010**, *35*, 73–79.
- (76) Johnson, C. J.; Levy, H. A. *International Tables for X-ray Crystallography*; Kynoch Press: Birmingham, 1974; Vol. IV.
- (77) CSD 1904224 contains the supplementary crystallographic data for model 4. These data can be obtained free of charge from FIZ Karlsruhe via [www.ccdc.cam.ac.uk/structures](http://www.ccdc.cam.ac.uk/structures).
- (78) Faulkner, R. A.; DiVerdi, J. A.; Yang, Y.; Kobayashi, T.; Maciel, G. E. The Surface of Nanoparticle Silicon as Studied by Solid-State NMR. *Materials* **2013**, *6*, 18–46.
- (79) Hart, G. L. W.; Forcade, R. W. Algorithm for generating derivative structures. *Phys. Rev. B* **2008**, *77*, No. 224115.
- (80) Yao, S.; Huhn, W. P.; Widom, M. Phase transitions of boron carbide: Pair interaction model of high carbon limit. *Solid State Sci.* **2015**, *47*, 21–26.
- (81) Shirai, K.; Sakuma, K.; Uemura, N. Theoretical study of the structure of boron carbide B<sub>13</sub>C<sub>2</sub>. *Phys. Rev. B* **2014**, *90*, No. 064109.
- (82) Rasim, K.; Ramlau, R.; Leithe-Jasper, A.; Mori, T.; Burkhardt, U.; Borrmann, H.; Schnelle, W.; Carbogno, C.; Scheffler, M.; Grin, Y. Local atomic arrangements and band structure of boron carbide. *Angew. Chem., Int. Ed.* **2018**, *57*, 6130–6135.
- (83) Ektarawong, A.; Simak, S. I.; Alling, B. Structural models of increasing complexity for icosahedral boron carbide with compositions throughout the single-phase region from first principles. *Phys. Rev. B* **2018**, *97*, No. 174104.
- (84) Ektarawong, A.; Simak, S. I.; Alling, B. Thermodynamic stability and properties of boron subnitrides from first principles. *Phys. Rev. B* **2017**, *95*, No. 064206.
- (85) Fischer, A.; Häussermann, U.; Scherer, W. Multi-center Bonding in Si<sub>4</sub> Rhomboid Rings – An Experimental and Theoretical Charge Density Study of β-SiB<sub>3</sub>, to be submitted for publication, 2019.
- (86) Werheit, H.; Filipov, V.; Kuhlmann, U.; Schwarz, U.; Armbrüster, M.; Leithe-Jasper, A.; Tanaka, T.; Higashi, I.; Lundström, T.; Gurin, V. N.; Korsukovam, M. M. Raman effect in icosahedral boron-rich solids. *Sci. Technol. Adv. Mater.* **2010**, *11*, No. 023001.
- (87) Vast, N.; Baroni, S.; Zerah, G.; Besson, J. M.; Polian, A.; Grinsditch, M.; Chervin, J. C. Lattice dynamics of icosahedral α-boron under pressure. *Phys. Rev. Lett.* **1997**, *78*, 693–696.
- (88) Tallant, D. R.; Aselage, T. L.; Campbell, A. N.; Emin, D. Boron carbide structure by Raman spectroscopy. *Phys. Rev. B* **1989**, *40*, 5649–5655.
- (89) Tallant, D. R.; Aselage, T. L.; Emin, D. Structure of icosahedral borides by Raman spectroscopy. *AIP Conf. Proc.* **1991**, *231*, 301–311.
- (90) Aselage, T. L.; Tallant, D. R.; Emin, D. Isotope dependencies of Raman spectra of B<sub>12</sub>As<sub>2</sub>, B<sub>12</sub>P<sub>2</sub>, B<sub>12</sub>O<sub>2</sub>, and B<sub>12+x</sub>C<sub>3-x</sub>: Bonding of intericosahedral chains. *Phys. Rev. B* **1997**, *56*, 3122–3129.
- (91) Wang, B.; Fan, Z.; Zhou, Q.; Xu, X.; Feng, M.; Cao, X.; Wang, Y. First principles calculations of the vibrational properties of icosahedral solid boron oxygen B<sub>12</sub>O<sub>2</sub>. *Phys. B: Condens. Matter* **2011**, *406*, 297–303.
- (92) Beckel, C. L.; Yousaf, M.; Fuka, M. Z.; Raja, S. Y.; Lu, N. Lattice vibrations of the icosahedral solid α-boron. *Phys. Rev. B* **1991**, *44*, 2535–2552.
- (93) Reshetniak, V. V.; Mavrin, B. N.; Edgar, J. H.; Whiteley, C. E.; Medvedev, V. V. Phonon states of B<sub>12</sub>P<sub>2</sub> crystals: Ab initio calculation and experiment. *J. Phys. Chem. Solids* **2017**, *110*, 248–253.
- (94) Aselage, T. L.; Tallant, D. R. Association of broad icosahedral Raman bands with substitutional disorder in SiB<sub>3</sub> and boron carbide. *Phys. Rev. B* **1998**, *57*, 2675–2678.